Van der Waals Epitaxy of the Transition Metal Dichalcogenide WTe_2

Master Thesis

Kevin Hauser

August 22, 2019

Kevin Hauser

Van der Waals Epitaxy of the Transition Metal Dichalcogenide WTe_2

Master Thesis, August 22, 2019

Supervisors: Dr. Christian E. Matt [†], Prof. Jennifer Hoffman [†] and Prof. Johan Chang [‡]

University of Zurich

Physics Department

Winterthurerstrasse 190

8057 Zurich

[†]Harvard University, Physics Department, 17 Oxford Street, Cambridge MA 02138

[‡]University of Zurich, Physics Department, Winterthurerstrasse 190, 8057 Zurich

Abstract

Transition metal dichalcogenides (TMD) are layered materials, which show a number of exotic physical properties, when synthesized as monolayer films. Therefore, monolayer TMDs are strong candidates for future technological applications such as spin or valleytronic-based devices or quantum computers[1,2]. To investigate and engineer these compounds, a controlled way of synthesis is required. Molecular beam epitaxy (MBE) has been widely employed to produce semiconducting devices with ultra-high purity[3]. In the case of TMDs, MBE-synthesized monolayers have been limited to islands with lateral size on the order of tens of nanometers due to big differences between the growth parameters of the transition metal and chalcogen such as sticking coefficient and surface diffusivity[4,5].

Here, I adapt a van der Waals epitaxy (vdWE) method[6,7] — based on providing the transition metal in the form of metal-organic precursors — with the goal to develop a growth recipe for WTe_2 monolayer films on highly-oriented pyrolytic graphite (HOPG) substrates. For this, I built a MBE system dedicated to metal-organic-precursor-based growth processes, which I used to conduct this growth study. Employing x-ray photoelectron spectroscopy (XPS), scanning electron microscopy (SEM), and atomic force microscopy (AFM), I characterized the as grown films and observed WTe_x-based, one-dimensional nanostructures at the step edges and two-dimensional islands on the terraces of the HOPG substrates. I argue that these two distinct film morphologies might be attributed to the formation of elemental W at the step edges and WTe_2 on the terraces, respectively.

This study presents a first step to extend the growth-dynamic improvements, as observed in the recently developed hybrid MBE method[8] — which revolutionized the MBE growth of oxide perovskites like titannates, ruthenates, stannates and vanadates[8–14] — into the field of TMD synthesis.

Zusammenfassung

Als Monolage synthetisierte Uebergangsmetalldichalkogenide (TMD) beherbergen eine Vielzahl physikalischer Eigenschaften, auf welchen Anwendungen in der *Valley*- und Spinktronik basieren könnten. Eine kontrollierbare, präzise Epitaxiemethode ist erforderlich, um diese Materialien zu kreieren und untersuchen. Molekularstrahlepitaxie (MBE) ist ein häufig verwendetes Verfahren für das Wachsen von hochreinen Halbleitern. Im Falle von TMDs sind MBE-gewachsene Monolagen jedoch limitiert auf kleine Flächen von wenigen Nanometern, bedingt durch die grosse Differenz der erforderlichen Prozessparameter für Chalcogen und Uebergangsmetall wie z.B. Haftungskoeffizient und Oberflächendiffusion.

In dieser Arbeit adaptiere ich ein Van der Waals Epitaxieverfahren, welches auf Metallorganischen Vorprodukten basiert, mit dem Ziel ein Rezept für das Wachsen von WTe_2 Monolagen auf hoch-orientiertem pyrolytischen Graphit (HOPG) Substraten zu wachsen. Dafür habe ich eine MBE Anlage gebaut, welche ausschliesslich auf das Wachsen von Schichten mit metalorganischen Vorprodukten ausgelegt ist. Mithilfe von Photoelektronenspektroskopie (XPS), Rasterelektronenmikroskopie (SEM) und Rasterkraftmikroskopie (AFM), zur Schichtcharakterisierung, konnte ich das Wachstum von eindimensionalen WTe_x Nanostrukturen an den Stufen des HOPG Substrats und zweidimensionalen, dünnen WTe_x Filmen auf den Substratterrassen untersuchen. Ich lege dar wie diese zwei unterschiedlichen Filmmorphologien zwei verschiedenen chemischen Phasen, elementarem W und WTe_2, zugeordnet werden können.

Diese wissenschaftliche Arbeit präsentiert den ersten Schritt zur Verbesserung der Wachstumskinetik, wie sie in der hMBE Methode — welche vor kurzem den Herstellungsprozess von *titanates*, *stannates*, *ruthenates* und *vanadates* revolutioniert hat — demonstriert wurde, im Feld der TMD Prozess Entwicklung.

Contents

1 Introduction

Low dimensional materials are at the forefront of modern condensed matter physics. Since the discovery of graphene and the pioneered exfoliation technique of Van der Waals (vdW) materials by A. Geim and K. Novoselov, people have been dreaming about stacking 2D materials like Lego blocks to compose heterostructures with novel electronic properties (see Fig. 1.1a) [15,16]. Scientists envisioned that such heterostructure could boost superconductivity by mimicking the layered structures of cuprates or replace silicone as the main resource for the semiconductor industry [17].

Among the group of vdW materials, the TMDs are of special interest due to the variety of physical phenomena they accommodate. To name a few: Superconductivity induced by pressure or ion-gating [18–23]; Ising-type superconductivity occurring in various TMDs [21,24,25] and its competition with the charge density wave order in $NbSe_2$ [26,27]; or the Quantum Spin Hall effect in monolayer 1T'-WTe_2 existing up to $100\,\mathrm{K}$ [28–32]. If interfaced with a superconductor, a QSH insulator is predicted to host Majorana fermions under broken time reversal symmetry [1] or if the superconducting order parameter has nodes [33,34]. Such Majorana modes could be utilized for fault tolerant quantum computation [35].

Despite the vast amount of research conducted on TMDs, fabrication of pristine monolayer films is still challenging. Three approaches are primarily used to fabricate TMD monolayers and heterostructures: *exfoliation*, where the monolayers are mechanically cleaved from a bulk crystal by using adhesive tape; *chemical vapor deposition* (CVD), where the layer forms out of a gaseous phase due to a chemical reaction [36 37]; and *molecular beam epitaxy* (MBE), where the constituents are provided in form of a molecular beam which allows controlled epitaxial layer-by-layer growth [5,30,38,39].

A large amount of research studies is performed on exfoliated TMD monolayers, since it doesn't require expensive equipment, but still allows to build few layer heterostructures like transistors or back-gated devices to test fundamental material properties [23,26,31,32,40–42]. However, the disadvantage of this fabrication process lays in the lack of scalability and reproducibility due to its trial-and-error nature. Furthermore, it only allows to control the environment to a limited extend (e.g. glove box with inert atmosphere) which can be detrimental for highly oxygen-sensitive

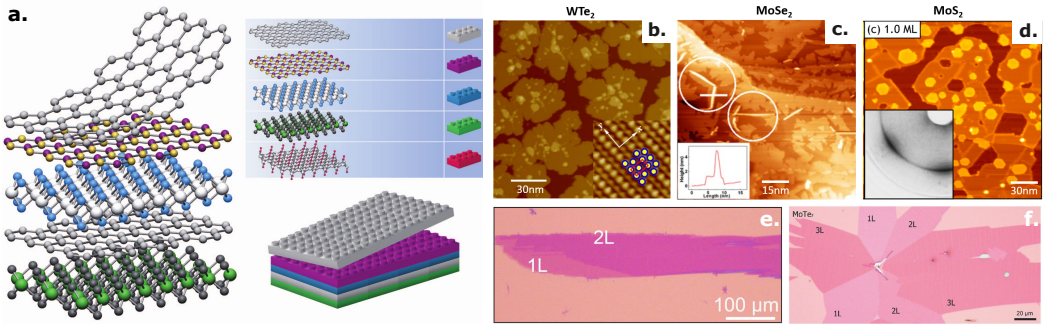

Fig. 1.1: **a** Pictorial graphic of composing a heterostructures from various 2D Van der Waals materials like Lego blocks. **b-d** Topographies acquired by scanning tunneling microscopy of MBE grown ultra-thin films (nominally close to one monolayer) of (b) 1T' WTe_2, (c) $MoSe_2$, and (d) MoS_2. In all samples island nucleation and a large defect and domain boundary concentration is observed suggesting insufficient surface diffusivity of the growth compounds. **e** and **f.** Topography of WTe_2 (e) and $MoTe_2$ (f) few-layer thin film grown by CVD; acquired using an optical microscope. From those images it is visible that monolayer flake sizes from CVD processes are up to three orders of magnitude larger than from MBE grown films. Adapted from 17, 39, 47–49.

compounds like monolayer of WTe_2 and $NbSe_2$ or heterostructures requiring pristine interfaces[43–46].

To achieve reproducible, ultra-clean films with atomically sharp interfaces, MBE is the preferred synthesis route. The growth process is performed in ultra-high vacuum (UHV) to reduce the impurity concentration. Low substrate temperatures furthermore allow for the growth of vertical heterostructures with minimal degradation or intermixing at the interfaces; and a slow growth rate ($1\,\text{Å}\text{min}^{-1}$) allows for precise thickness control[5,38]. However, MBE relies on thermal evaporation to create the molecular beam which poses difficulties for the refractory metals (e.g. W, Mo, Nb) due to their low vapor pressure. Therefore, the standard technique of using a Knudsen cell is not applicable and electron-beam (e-beam) evaporators are required, instead. One of the major shortcomings of e-beam evaporators is their flux instability. Due to the slow growth rate of MBE such flux instabilities lead to stoichiometric variations, which are enhanced by the high sticking coefficient of the refractory metals, resulting in reduced film quality and small patch sizes[5,7,39]. This problem is not present in CVD grown TMDs, where μm monolayer patch sizes for a broad range of TMDs are achievable[4,49–52]. The shortcoming of CVD, is that the chemical reaction takes place in an ambient-pressure or low-vacuum environment. This can pose problems for the study of impurity sensitive phenomena of topological phases or interface effects requiring pristine films

A solution to these issues was presented by Tiefenbach *et. al.*, who developed a CVD-related, MBE-growth process for WS_2 on vdW substrates[6,7,53]. In this process – taking place in an UHV environment — the refractory metal is provided by a metal-

organic precursor (i.e. $W(CO)_6$) instead of an e-beam. This method combines the benefit of both deposition techniques: the precise and clean layer-by-layer growth ability from MBE systems with the enhanced surface mobility of refractory metals in metal-organic-precursor-based CVD processes.

The research groups of Roman Engel-Herbert and Bharat Jalan recently established a similar metal-organic-precursor-based growth approach for a different group of materials — the oxide perovskites — and coined the term *hybrid MBE* (hMBE) for it. They demonstrated the capabilities of hMBE for oxide perovskites by growing high-quality films of TiO_2, $SrTiO_3$, $SrVO_3$, Sr_2RuO_4, and $BaSnO_3$ which are challenging to grow by conventional MBE[9–12,14]. In their studies they could show a drastic widening of the growth window due to the increased surface mobility of the non-volatile metals (Ti, Sn, V, Ru), provided by metal-organic precursors. The existence of such growth windows allows for a stoichiometric film growth, which is robust against fluctuations in the reactants concentration[10,12,14].

Employing metal-organic precursor — based on the work of Tiefenbach *et. al.* — I aim to lay the foundation for an advancement in TMD synthesis with the hope to enhance the research of the physical phenomena emerging from vdW-heterostructural systems.

2 Physics of Transition Metal Dichalcogenides

2.1 Crystal Structure

TMDs can be described by the generalized formula MX_2 where M stands for the transition metals and X represents the chalcogen atoms (e.g. S, Se, Te). The variety of possible combinations (see Fig. 2.1 a) of elements leads to dozens of different materials hosting exotic physics like superconductivity, charge density waves, spin splitting of the electronic bands or topological phases[54]. Group IV-VII TMDs are arranged in a layered structure where each layer consists of a plane of metal atoms sandwiched by two planes of chalcogen atoms with a typical layer height of 6 to 7 Å. The chalcogens atoms of these X-M-X stacked layers have no dangling inter-layer bonds leading to a van der Waals interface between adjacent layers in bulk TMDs resulting in a two-dimensional electronic structure of these materials. This difference in bonding strength between in-plane (covalent) and out-of-plane (van der Waals) makes these materials easy cleavable and therefore suitable for heterostructure fabrication by exfoliation. TMDs can form in several structural phases due to different coordination spheres of the transition metal atoms. The most common polymorphs are the 2H (trigonal prismatic metal coordination) phase[37] and the 1T (octahedral metal coordination) phase. For the 1T phase there exist two distorted structures, the monoclinic 1T' phase, and the non-centrosymmetric $1T_d$ phase which share the same in-plane crystal structure but differ in their stacking order.[55,56]. The digit indicates the number of layers (units of M-X-M) per unit cell. The 2H phase can be understand as three planes of hexagonally arranged atoms in a ABA stacking, whereas the 1T phase follows an ABC stacking scheme. This is visible in the top view of Fig. 2.1 b, where the lower-lying chalcogene atoms are not visible for the 1H phase. For most of the group VI TMDs the 2H phase is thermodynamically stable and the 1T phase is metastable, whereby bulk WTe_2 is an exception and favors the $1T_d$ phase at room temperature[54]. The free-standing 1T phase is not stable and undergoes a spontaneous lattice distortion into the 1T' phase by doubling the periodicity in the x direction causing the metal atoms to form a 1D zigzag chains along the y direction, as indicated by the blue dashed line in Fig. 2.1 d

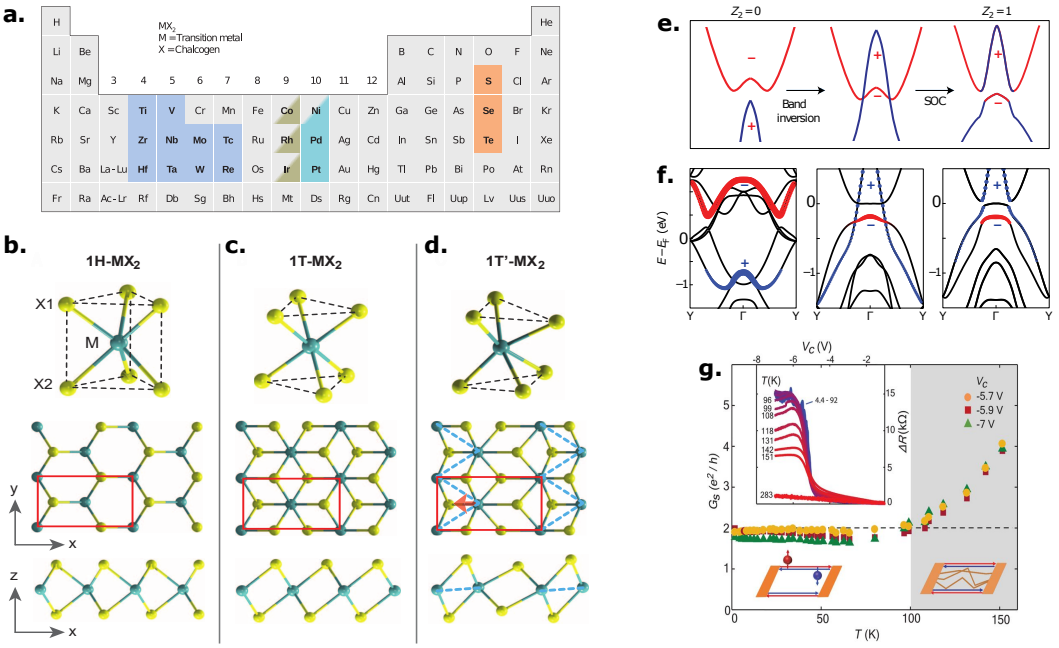

Fig. 2.1: **a** the periodic table highlights the Metals (blue) and chalcogens (orange) which can form transition metal dichalcogenides based on the structural formula MX_2. The combination of these elements can form over 40 different TMD compounds. The partly highlighted elements (Co, Rh, Ir, Ni) only from with some of the chalcogenides layered structures. b -d Stick and ball model of the different polymorphic phases. azure colored balls refers to the metal atoms and yellow ones refers to the chalcogens. The unit cell is indicated in red. **e** Schematic diagram shows the evolution from a normal band structure to a topological non-trivial band structure due to band inversion and a bulk band gap opening due to spin-orbit coupling (SOC). f Calculated band structure to show the evolution for the case of 1T' WTe_2. g Conductivity measurement shows the quantized edge conductance e^2/h up to $100\,\mathrm{K}$. Adapted from 28–30, 37.

2.2 The 1T'-WTe_2 Quantum Spin Hall Phase

The quantum spin hall phase was predicted to occur in monolayer 1T' WTe_2 by Qian *et. al.*[28] in 2014. Qian *et. al.* argued that the lattice distortion from the 1T to the 1T' phase in monolayer (ML) WTe_2 causes a band inversion between the chalcogenide-p and metal-d bands, as indicated in Fig. 2.1 e-f, rendering the band structure topologically non-trivial. Strong spin-orbit coupling then lifts the degeneracy at the band crossing point, opening a bulk band gap.

As first indication of the existence of the QSH phase in 1T' WTe_2 were presented by Fei *et. al.*[31] showing insulating bulk and edge conductance by transport measurements on 1T' WTe_2 exfoliated heterostructure devices and by Tang *et. al.*[30], reporting the band inversion and a band-gap opening due to spin-orbit coupling by APRES and STM measurement on MBE-grown ML 1T' WTe_2. The final proof — the measurement of the quantized edge conductance of e^2/h — was provided by Wu *et. al*[29] showing that the QSH phase exists up to $100\,\mathrm{K}$ by transport measurements

on exfoliated monolayer 1T' WTe_2. Further evidence was provided so far by STM and microwave impedance microscopy directly resolving the edge conductance of monolayer 1T' WTe_2 flakes[57,58].

With the confirmation of the QSH phase existing up to $100\,\mathrm{K}$, WTe_2 provides an promising platform for the realization of heterostructures hosting topological superconductivity. In the next section I will briefly introduce theoretical predictions for the existence of emergent Majorana in ML 1T' WTe_2-based heterostructures.

2.3 Prospective WTe_2-based Heterostructures

A promising route to implement quantum computation proposes to utilize the non-Abelian braiding properties of Majorana zero modes (MZMs) as the building block of fault-tolerant qubits[35]. Many proposals have focused on heterostructures between conventional or high-temperature superconductors and three dimensional topological insulators (3D TIs), in which superconductivity is proximity-induced into the 3D TI. In such systems, single MZMs are predicted if time-reversal symmetry is broken. This is usually achieved by introducing magnetic dopants or applying an external magnetic field[1,59]. However, the experimental realization of MZMs in 3D TI-SC heterostructures turns out to be challenging because conventional s-wave superconductors have a low T_c making it difficult to detect and study MZMs. High-temperature superconductors, like Bi-2212, can have a T_c above $100\,\mathrm{K}$[60], but have short out-of-plane coherence lengths that constrain the proximity-induced superconductivity to a few atomic layers, which is not sufficient for a 3D TI to fully develop its protected surface states[61,62]. These conflicting requirements for length scales as well as the additional requirement of broken time reversal symmetry has lead to failed attempts in the search for Majorana-hosting heterostructures of 3D TIs and high-temperature superconductors[62].

An interesting alternative is provided by recent proposals that predicts the existence of Majorana Kramer pairs (MKP) at the corner of 2D QSH islands on top of a superconductor with a sign-changing order parameter, such as cuprates (d-wave) or iron-pnictides ($s_\pm$)[33,34]. The helical edge states of the QSH insulator, described as 1D massless Dirac fermions, are gapped out by the induced superconducting gap, which introduces a Dirac mass . The Dirac mass undergoes a sign change at the corner of the 2D film — due to the pairing symmetry of the superconductor — which acts as a generator for MKPs as domain wall excitations. ML 1T' $WTe_2$is a strong

candidate to test such a proposal due to its high-temperature QSH phase (up to $100\,\mathrm{K}$ and provide therefore a viable system to study emergent Majorana physics

3 Methodology

3.1 Molecular Beam Epitaxy

3.1.1 Conventional MBE

The characterizing feature of the MBE growth technique is the beam-like nature of the mass flow towards the substrate which, allows a layer-by-layer growth were the film composition can be varied on a monolayer scale. MBE is necessarily a UHV process for to two reasons: (1) to sustain a molecular beam the mean free path of the gas molecules needs to be larger than the distance between effusion cell and substrate; (2) the slow growth rates of MBE processes require low impingement rates of residual gas species on the substrate surface to sustain a low-enough defect density in the grown film. Therefore, for growth rates around $\mu\mathrm{m/h}$ a residual gas pressure in the UHV is required[63].

A typical MBE system — shown in Fig. 3.1 a — consists of Knudsen effusion cells, which provide the film constituents by thermal evaporation in the form of a molecular beam, and the substrate holder which is located at the focal point of all the installed effusion cells. Diagnostic tools generally used to support the film deposition include reflection high-energy electron diffraction (RHEED), which allows to monitor the film crystallinity, growth rate and crystal orientation on the substrate during the growth; residual gas analyzer (RGA), which measures the partial pressure of the gaseous species present in the chamber; and quartz crystal microbalance (QCM), which are used to calibrate the effusion cell flux rates.

An important concept in molecular beam epitaxy is the *adsorption-controlled growth window*, which refers to growth conditions in which stoichiometric films are deposited insensitive to flux small variations. I will further elaborate on this effect using the example of the well understood growth process of GaAs. For the GaAs growth there exists a substrate temperature range where As is only present in its gaseous phase while the decomposition temperature for GaAs is not reached yet, i.e. solid GaAs forms, liquid Ga is accumulating at the surface, and gaseous As evaporates off the surface. This region in process parameter phase space is bound by the As-condensation equilibrium line at the lower-temperature end and by the

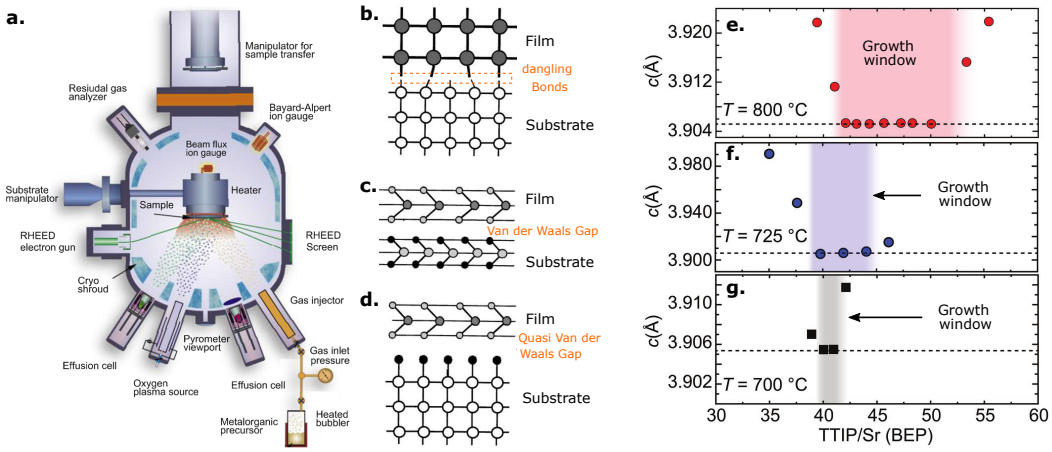

Fig. 3.1: **a** Schematics of a typical MBE system. Its main components are the substrate manipulator with integrated heater to control the substrate temperature and the effusion cells. If the deposition process employs precursor or a reactive oxygen environment a gas injector or oxygen plasma source are included, too. **b-d** Interfaces between different combinations of two and three-dimensional substrates to to illustrate the relaxation of the lattice-matching condition for van der Waals interfaces. **e-f** Substrate temperature evolution of the out-of-plane lattice parameter c plotted against the precursor-Sr concentration ratio for the epitaxial $SrTiO_3$ film shows the opening of a growth window (shaede region) for increased temperatures. Adapted from 10, 64, 65.

GaAs-decomposition equilibrium line at the higher-temperature end. Under this condition GaAs forms stoichiometrically and is insensitive to Ga fluctuations as long as an excess of As is provided[3,8] This region in process parameters space spans roughly over nine orders of magnitude in As partial pressure, allowing the growth of pristine GaAs films. This example demonstrates that the existence of an adsorption-controlled growth window is highly advantageous for the growth of high-quality crystalline films and significantly lowers the stability requirements for beam-flux substrate temperature.

3.1.2 Van der Waals Epitaxy

Van der Waals Epitaxy — coined in 1984 by Koma *et. al.*[66] — refers to the epitaxial growth of two dimensional materials such as TMDs on each other or on passivated three-dimensional substrates[5,67]. It differens from conventional MBE in the way that the interlayer vdW bonding strength is much weaker than the intralayer co-valent bonds. This leads to interesting effects: The large difference in strength between the in-plane and out-of-plane bonding strongly relaxes the lattice-matching condition, allowing a much larger variety of combinations between substrates and films[5,6,65,68]. The growth of heterostructures with lattice mismatches up to $58\,\%$ has been demonstrated reported[69].

The differences of interfaces formed by two and three-dimensional materials is pictorially drawn in Fig. 3.1 b-d. In panel b, We see how for two three-dimensional materials the requirement for the bond formation of the mismatching lattices at the interface induces strain into the first layers of the film. The epilayer atoms have to find the energetically favorable situation by maximizing the number of bonds while minimizing lattice strain. The consequence of the large lattice mismatch is that the adhesion of the film on the substrate is minimized due to the lack of bonds to the substrate or that the film does not form in a coherent crystalline phase due to the lack intralayer bonds. This, in general, poses a significant restriction on the design of heterostructures of three-dimensional materials. In panel c, on the contrary, I see an interface formed by vdW materials where the weak interlayer (vdW) coupling allows for an unstrained growth up to large lattice mismatches. As illustrated in panel d, it is also possible to grow two-dimensional materials strain-free on three-dimensional substrates if the dangling bonds from the substrate are passivated. This was shown for the growth of TMDs on the sulfur-terminated surfaces of GaAs(111) and flour-terminated surfaces of CaF_2 [67,70].

3.1.3 Hybrid MBE

hMBE refers to the deposition process of oxide perovskites by combining elemental MBE sources with oxygen and metal-organic precursors. Recent studies by the research groups of Prof. B. Jalan and Prof. R. Engel-Herbert established adsorption controlled growth windows for titanates, stannates and vanadates [9,10,12–14] I will briefly discuss the challenges and advances in this field of epitaxial-layer synthesis as the concepts of growth dynamics are also applicable to my study.

I will shortly outline the advances of introducing metal-organic precursors for perovskite oxides using $SrTiO_3$ as an example. For elemental source MBE, an estimation for an adsorption-controlled growth window of $SrTiO_3$ can be adapted from the well-understood growth mechanism of GaAs, where Ti and SrO play the role of Ga and As. Since Ti is assumed to have a sticking coefficient of 1, it is the volatility of SrO which defines the boundaries of the growth window. However, due to the low vapor pressure of SrO the adsorption-controlled growth region lays at such low flux rates and high substrate temperatures that it is not experimentally accessible with current MBE systems [8,64]. The lack of a adsorption-controlled growth window requires precise control of constituents concentration during the growth, which is challenging if electron-beam evaporators are employed, due to their inferior flux stability [64].

Providing the a metal compound in the form of a organic precursor (e.g. titanium tetra isopropoxide (TTIP)) increases the surface mobility and volatility of the metal compound (as long as it is bound to an organic molecule) due to the lower adsorption energy of organic molecules on the substrate. Experiments indicated that the resulting changes in surface kinetics lead to a new growth window, which is now defined by the volatility of the precursor molecule instead of the SrO (see Fig. 3.1 eg)[8,64]. A rigorous theoretical understanding of this $SrTiO_3$ growth process is still missing, due to the complexity of the growth dynamics[8]. In this way the application of metal-organic precursor provides a route to adsorption-controlled growth techniques. Nevertheless, these experimental results show that application of metal-organic precursors could present a promising route to develop a adsorption-controlled growth window for many more material classes.

3.2 Film Characterization

3.2.1 X-ray Photoelectron Spectroscopy

X-ray photoelectron spectroscopy (XPS) is based on the photoelectric effect where electrons, that are excited by absorbing an incoming photon, escape the sample[71,72]. By measuring the kinetic energy E_{kin} of the escaping electrons and considering energy conservation

$$E_{kin} = \hbar\omega - \phi - |E_B| \tag{3.1}$$

it is possible to deduce the binding energy E_B of the electron in its initial state. Here $\hbar\omega$ refers to the energy of the incoming photon and ϕ refers to the work function of the sample. In this way, XPS provides access to the chemical composition by resolving the element-specific core-electron energy levels. For crystalline samples, it further allows to characterize the chemical environment of specific elements by quantifying a shift of their core-level[73]. For example, the W core levels in WO_3 are slightly shifted, compared to their position in elemental W[74]. The probing depth in XPS is restricted by the inelastic scattering of electrons inside the sample. The probability for the electrons to undergo inelastic scattering depends on their kinetic energy when escaping the sample and is characterized by the inelastic mean-free path[75]. For my applied photon energies, the inelastic mean-free path is in the range of 10 Å to 20 Å.

I will now outline the calculation I made to compute the composition ratio of W to Te and W to WO_3. Following the derivation presented by Powell[76], the measured photoelectron current can be written as

$$I_s(E_i, X) = AN_i\sigma_i(\hbar\omega, \vartheta, X)\lambda_s(E_i)H(E_i) \tag{3.2}$$

with kinetic energy E_i, X of the level X and the i^{th} species from sample s. The factor A describes the x-ray flux on the sample and geometrical factors concerning the incoming photons and analyzed electrons into account; N_i refers to the volume density of atoms of the i^{th} species; $\sigma_i(\hbar\omega, \vartheta, X)$ is the differential cross section for the shell X of the i^{th} species at the x-ray energy $\hbar\omega$ and for the electron ejection angle ϑ; $\lambda_s(E_i)$ is the inelastic mean-free path in the sample for electrons with kinetic energy E_i; and $H(E_i)$ is a property of the analyzer system and consists of the analyzer transmission function and the detector efficiency. Furthermore, I can write for the differential cross section

$$\sigma_i(\hbar\omega, \vartheta, X) \quad \propto \quad \sigma_i(\hbar\omega, X)F(\vartheta, X, \bar{\hbar}) \tag{3.3}$$

where $\sigma_i(\hbar\omega, X)$ is the total cross section for photoionization from level X by x-rays with energy $\hbar\omega$, and $F(\vartheta, X, \hbar\omega)$ is an angular asymmetry factor. Since I have $\vartheta = 90°$ in my measurement, I can write $F(\vartheta = 90°, X, \hbar\omega) = 1 + \beta(X, \hbar\omega)/4$ with $\beta(X, \hbar\omega)$ being an asymmetry parameter which is tabulated and can be looked up.

Having set up the framework I can now focus on my specific case. For comparing the chemical ratio between W and WO_3 I can simplify eq. 3.3: since I compare two peaks from the same atom and the same transition (i.e. the W $4f_{7/2}$ transition for W and WO_3) I can assume that A and $H(E_i)$ are similar for both measured intensities. Therefore I can write

$$\frac{I_{\text{WO3}}(E_{\text{WO}_3,4f})}{I_{\text{W},4f}(E_{\text{W},4f})} \quad \simeq \quad \frac{N_{\text{WO}_3}}{N_{\text{W}}} \tag{3.4}$$

where I assumed that the inelastic mean-free path λ is equal for electrons from both core level peaks. I see that the compositional ratio can directly be derived from the ratio of the measured current of photoelectrons.

For comparing the ratios between different elements (i.e. Te and W), I have to take the differential cross section of the individual core level peaks into account. I furher

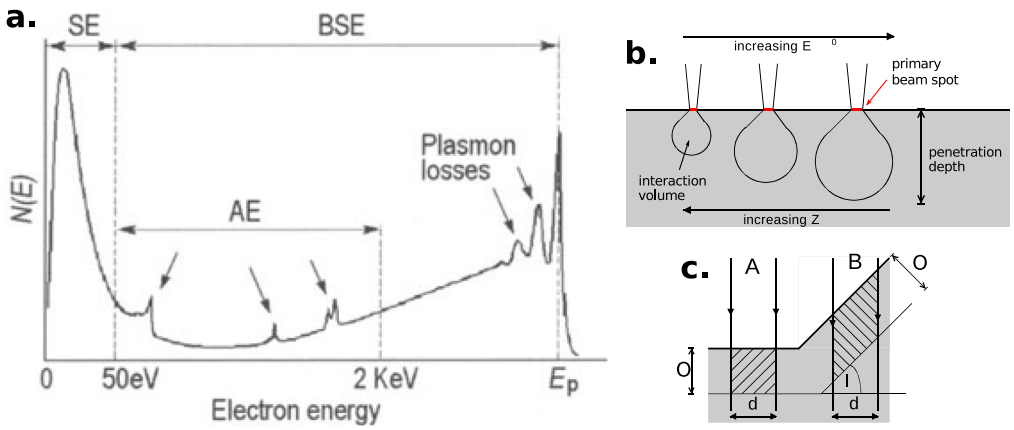

Fig. 3.2: **a** Energy spectrum of electrons emitted from the sample which is irradiated by primary electrons with energy E_p. Characteristic energy ranges for the SE and BSE are indicated. **b** Pictorial representation of the interaction volume from which BSE are emitted and its dependence on primary electron energy E_0 and atomic number Z. Indicated in red is the primary beam-spot size from which the SE originate. **c** Schematic drawing of a sample surface irradiated by beam A and B to illustrate the increase in volume from which SE escape by changing the incidence angle of the primary electrons. Adapted from 77, 78.

assume that A and $H(E_i)$ do not differ significantly and cancel out. Therfore, for eq. 3.3 I get

$$\frac{I_{\mathrm{Te},3d}(E_{\mathrm{Te},3d})}{I_{\mathrm{W},4f}(E_{\mathrm{W},4f})} \simeq \frac{N_{\mathrm{Te},3d}\sigma_{\mathrm{Te}}(\hbar\omega, 3d)\,[1+\beta(3d,\hbar\omega)/4]\,\lambda(E_{\mathrm{Te},3d})}{N_{\mathrm{W},4f}\sigma_{\mathrm{W}}(\hbar\omega, 4f)\,[1+\beta(4f,\hbar\omega)/4]\,\lambda(E_{\mathrm{W},4f})} \tag{3.5}$$

The XPS measurements presented in this work were performed on a Thermo Fischer K-alpha XPS system. This system utilizes a monochromatic soft Al Kα x-ray beam with a beam energy of $1.4866\,\mathrm{keV}$ and a line width of $0.3\,\mathrm{eV}$ leading to an experimental resolution of $0.03\,\mathrm{eV}$.

3.2.2 Scanning Electron Microscopy

In scanning electron microscopy a beam of primary electrons with an electron energy E_p between $1\,\mathrm{keV}$ and $15\,\mathrm{keV}$ is focused onto the surface of a specimen causing the emission of electrons. Scanning the beam in a raster across the sample allows for recording topographical images of the surface, where probing depth and spatial resolution are related by the kinetic energy of the primary electrons. Regarding the emitted electron energy spectrum (shown in Fig. 3.2 a), I distinguish between two types of emitted electrons which contain different information about the surface: secondary electrons (SE), present at low energies, and backscattered

electrons (BSE), spanning the range form the primary-electron energy E_p down to low electron energies.

SE are low energy electrons (0 to $50\,\mathrm{eV}$) with a narrow escape depth ($< 2\,\mathrm{nm}$) due to inelastic scattering inside the specimen. They mainly originate within the primary beam spot (see Fig. 3.2 b), resulting in a high surface sensitivity and a high spatial resolution in the nm range. The yield δ of SE depends on the primary electron energy E_p and angle φ between incoming primary electron and the surface. Since primary electrons with higher energy undergo less scattering in the topmost layers (i.e producing less SE), δ decreases with increasing E_p. In this sense, there is a trade-off when optimizing the spatial resolution by increasing E_p since this reduces the signal-to-noise ratio by decreasing φ. The reason for the yield-depending angle of the incoming electrons is illustrated in Fig. 3.2 b. The volume from which SE can escape into vacuum — depending on the escape depth O — increases with decreasing incidence angle. In this sense steep regions on SEM images appear much brighter than flat images, as seem in the image of the three-dimensional nanostructures on my substrates (see Fig. 5.7 and Fig. 5.6).

Backscattered electrons (BSE) are primary electrons that are ejected from the specimen by scattering through an angle greater than $90°$[78]. The energy loss during back scattering is small leading to high kinetic energies for BSE. The cross section for backscattering is proportional to Z^2 (Z is the atomic number) allowing me to characterize spatial variations in the chemical composition. However, due to the higher kinetic energy, the escape depth of BSE is much larger than for SE — for E_p above $3\,\mathrm{keV}$ the escape depth can become tens or hundreds of nanometer[78]. This makes chemical analysis studies of monolayer films employing BSE generally difficult.

The SEM measurements were performed at a Zeiss FE-SEM Ultra Plus system. All images were recorded at a working distance of $10\,\mathrm{mm}$ with an electron beam energy of $5\,\mathrm{keV}$.

3.2.3 Atomic Force Microscopy

Atomic force microscopy is based on measuring the inter-atomic forces between a sharp tip at the end of a cantilever and a sample surface. The measurement setup is indicated in Fig. 3.3 a and consists of cantilever with tip, xyz-piezo motors to move the sample, and mechanism to measure the cantilever deflection. In the illustration it is done optically by tracking the displacement of a focused laser with a CCD sensor.

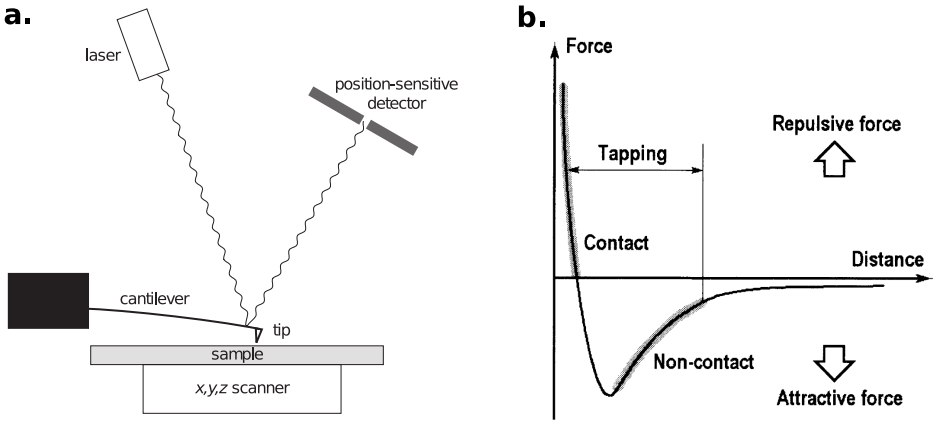

Fig. 3.3: **a** Schematics of the AFM measurement principle: A cantilever with a tip of the size of a couple of nanometer is scanned over a sample while the cantilever deflection is measured optically by the displacement of a laser on a CCD sensor. **b** Characteristic force-distance curve for an AFM tip in front of a sample. Adapted from 77, 79.

Inter-atomic forces are measured by recording the deflection of the cantilever while scanning the tip across the sample to gain topographical information[77,79].

The tip-sample interaction is described by the force-distance curve illustrated in Fig. 3.3 b. The shape of this curve is given by attractive van der Waals forces at higher distances and repulsion due to the the Pauli exclusion principle at very short distance.

As indicated in the force-distance curve (Fig. 3.3 a) three different modes of operation can be distinguished: contact mode, non-contact mode, and tapping mode. Contact mode uses a static cantilever operated in the repulsive regime where the tip-sample separation is only a few Å. This mode is used for constant height or constant force measurements. In amplitude-modulated (AM) non-contact and tapping mode the cantilever is kept vibrating at a frequency close to its resonance frequency. Since the resonance frequency depends on the coupling between tip and sample, changes in the surface topography will shift the resonance frequency, causing the amplitude of vibration to change. Changes in the amplitude provide a measure of the surface topography[79]. The difference between non-contact mode and tapping mode is the sample distance — tapping mode *touches* the sample as the name implies it. An advantage of AM-AFM over contact-mode AFM is the possibility to gain compositional or roughness information of the surface from phase contrast images[80,81]

In the scope of this thesis I used the AM-AFM tapping-mode measurement technique to gain height information of the grown structures. I further resolved differences in the chemical composition on the surface from phase-contrast analysis[81]. All

measurements were performed on a Cypher AFM from Asylum Research by using Si cantilever (AC160TS-R3)[82] with a resonance frequency of $300\,\mathrm{kHz}$, a spring constant of $26\,\mathrm{N\,m^{-1}}$, and a tip radius of $7\,\mathrm{nm}$.

4 Experiment

4.1 Setup

To conduct the metal-organic growth study I developed and built an MBE system dedicated for this purpose. The necessity to build such a system from scratch comes from the fact that the process employs the decomposition of metal organic precursors. Due to the high cleanliness standards for MBE growth chambers and the needs of keeping them from any possible contamination, it would have been risky to introduce a metal-organic precursor into the existing non-organic chalcogenide MBE chamber from the Hoffman lab.

My system consists of a main chamber and a load lock chamber (LL) separated by a manual gate valve (Fig. 4.1a). The main chamber is equipped with a Turbo molecular pump backed by an oil-free scroll pump. The pressure in the LL is measured by a full-range gauge (Pfeiffer PKR 251) and in the main chamber by a hot-cathode Bayard-Alpert gauge (Varian glass tub ion gauge 571). Hot cathode gauges are preferred in MBE systems because the hot filament reduces gauge degradation caused by contamination through the reactant. It was possible to establish a pressure in the $10^{-8}\,\mathrm{mbar}$ range by pumping over several days and without baking out [†]. A transfer system with a self-designed sample grabber customized for omicron-flag-style sample holder allows in-situ sample transfer from the LL to the heater stage inside the main chamber. In this fashion I'm able to continuously perform growth cycles without venting the system for sample exchange. The sample temperature during deposition is continuously monitored with a pyrometer (LumaSense IGA6 Advanced). To introduce the reactants into the chamber (i.e. Te and $W(CO)_6$) I built an effusion cell and a precursor inlet system. The inside of the chamber with three main components (e.g. the heater stage, precursor inlet, and effusion cell) is shown Fig. 4.1b.

[†] Normal base pressures before growth started, however, were normally in the $10^{-7}\,\mathrm{mbar}$ range

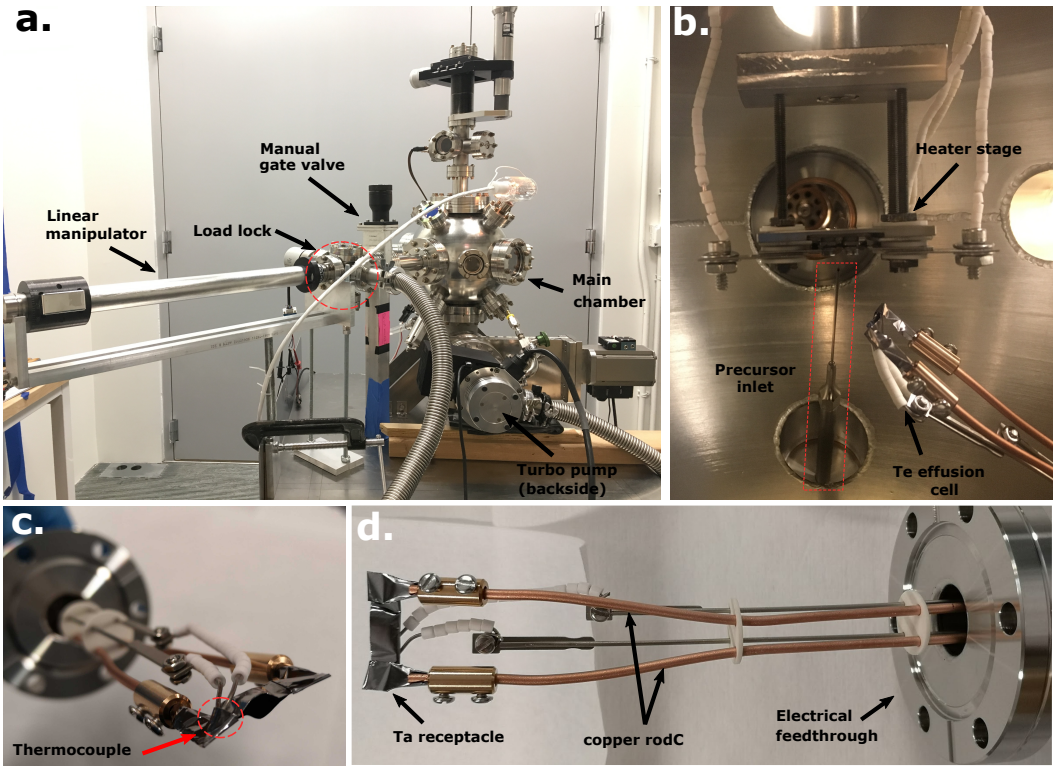

Fig. 4.1: **a** Outside view of the designed MBE system. Visible parts are the linear manipulator, the load lock, the manual gate vale, and the main chamber. **b** inside view of the main chamber. Visible parts are the heater stage (upper part), the effusion cell (right side), and the transfer line from the precursor inlet system (lower center, highlighed by the red dashed box). Worth noting here is how close the nozzle is mounted to the sample to ensure a high precursor concentration. **c** and **d** show the effusion cell with its main components labelled. The opening in the Ta receptacle clearly visible in c is pointed towards the sample stage when mounted to ensure an optimal Te flux.

4.1.1 Heater Stage and Sample Holder

To control the sample temperature during the deposition process I designed a heater stage and sample holder for direct current heating (i.e. resistive heating by passing a current through the sample). This is preferable compared to indirect-current heating (e.g. by a filament behind the sample). It ensures that the hottest point in the setup is always at (or close to) the sample, therefore limiting contamination through hot, outgasing chamber components and ensuring that the precursor decomposition mainly takes place at the sample.

The main components of the sample holder and heater stage are made from Haynes 214 — a Ni-Cr-based high-temperature oxygen-resistant alloy[83]. To achieve electrical isolation between the different parts of the sample holder and heater stage — which is necessary to allow a current to pass through the sample — Alumina washer have been used (Fig. 4.2 b and d). The assemblies for heater stage (Fig. 4.2a) and sample

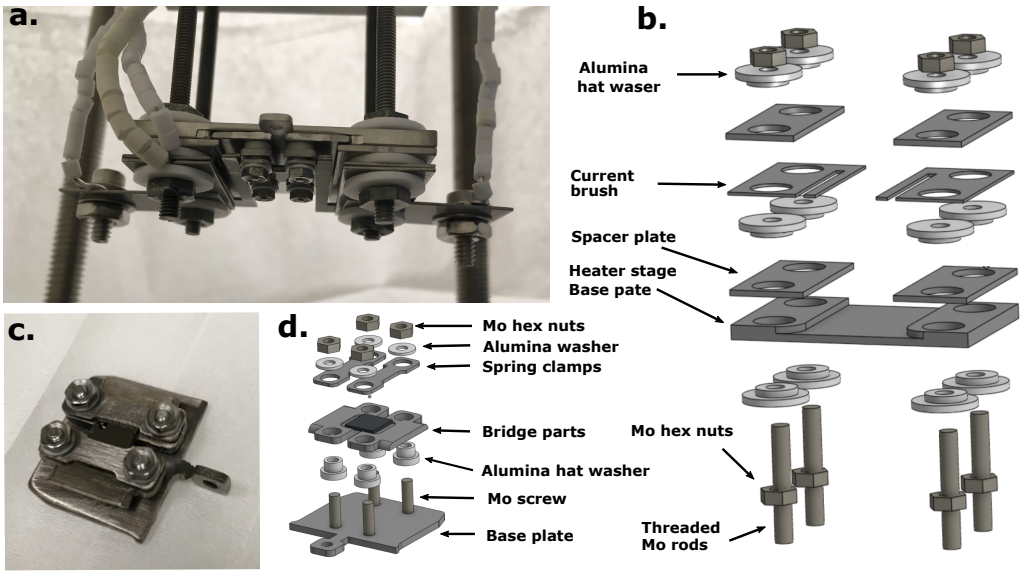

Fig. 4.2: **a** Assembled heater stage with sample holder inserted. Wires covered in Alumina beads at the side provide the current and the two wires in the front correspond to a thermocouple. **b** schematic of the heater stage shows the layered designed. **c** Sample holder with sample mounted. The spring clamps cover the sides of the HOPG sample allowing film growth only in the center. **d** from the exploded-view drawing of the sample holder it is visible how the clamping mechanism works: the HOPG sample is pressed into a grove in the bridge parts by the spring clamps. To increase the heating efficiency we included a SiC sample between bridge parts and HOPG as discussed in the text (not shown here).

holder (Fig. 4.2b) are composed of layers of Haynes and Alumina washers which are held together by threaded molybdenum parts (rods, screws, and hex nuts), as illustrated by the exploded-view drawings Fig. 4.2c-d.

As HOPG is a good conductor (i.e. resistive heating is inefficient), I had to add a heater plate on the back-side of the HOPG. For this I used a 6H silicon carbide (SiC) plate due to its higher resistivity and good thermal conductivity. The SiC surface facing the HOPG was polished to increase contact resistance. This high contact resistance redirects the current through the SiC plate causing it to be homogeneously heated up; while the contact pressure form the clamping mechanism ensures a good thermal conductance to the HOPG leading to an evenly distributed heat transfer across the contact surface.

4.1.2 Effusion Cell Design

To provide Te to the substrate I built a direct current heated effusion cell as depicted in Fig. 4.1c and d. It consists of a CF-flanged electrical feedthrough with two copper rods and two k-type thermocouple connections extending into the chamber. Between

the two copper extensions, I mounted a cup-shaped Ta foil, acting as a receptacle for the Te. The Te is then sublimated by passing a current through the copper rods heating up the Ta receptacle. A k-type thermocouple, mounted to the receptacle (see label in Fig. 4.1c), ensures temperature control.

This simplistic and cost-effective design meets the basic requirements for a chalcogenide effusion cell but reveals some shortcomings. During operation a temperature gradient exists across the receptacle — caused by the thermocouple, which is touching the Ta foil on one side (Fig. 4.1c) and acting as a heat sink. I expect the temperature differences to be as high as $50\,^{\circ}\mathrm{C}$ in the range of my operation temperatures. Since the colder side is always located around the thermocouple-receptacle junction, the measured temperature values in my study are an underestimation of the actual receptacle temperature. However, this phenomena was very reproducible and I expect that it introduces a systematic temperature offset error which is the same for all conducted growths and does therefore not affect the reproducibility of the Te flux.

4.1.3 Precursor Inlet

$W(CO)_6$ has a high vapor pressure ($2 \times 10^{-3}\,\mathrm{mbar}$ at $30\,^{\circ}\mathrm{C}$[84]) and sublimates easily at ambient temperatures. For this reason I can introduce the precursor into the chamber without additional heating. The precursor inlet system consists of a high precision leak valve separating a Pyrex glass tube from the main chamber. Inside the main chamber, I installed a tubing system, directing the precursor to the sample (see lower center in Fig. 4.1b). The leak valve allows to adjust the precursor flux to regulate the precursor partial pressure inside the main chamber. To avoid precursor condensation at the metal walls inside the tubing system I keep the dosage valve and the adjacent chamber walls at elevated temperature ($\approx 50\,^{\circ}\mathrm{C}$), during the growth process. At the same time, the Pyrex tube is placed in a water bath to keep the precursor at room temperature.

4.2 Growth Process

The systematic growth study presented in this thesis is split into two series, each performed at a specific Te effusion cell temperature of $275\,^{\circ}\mathrm{C}$ (series one) and $325\,^{\circ}\mathrm{C}$ (series two). Each growth study is split in two grow series for the effusion cell

temperatures $275\,°\mathrm{C}$ and $325\,°\mathrm{C}$. One series consists of multiple growths at different substrate temperatures: $500\,°\mathrm{C}$ to $700\,°\mathrm{C}$ for series one and $475\,°\mathrm{C}$ to $625\,°\mathrm{C}$ for series two. The $W(CO)_6$ precursor flux and the deposition time were kept constant for all growths. I used air-cleaved HOPG as my substrate. The Te effusion cell and the $W(CO)_6$ precursor glass tube were filled once at the beginning of the entire study. I used high-purity Te granules ($99.9999\,\%$) from Alfa Aesar and high-purity $W(CO)_6$ ($99.99\,\%$) from Sigma Aldrich. I filled the $W(CO)_6$ into the Pyrex tube under ambient atmosphere. No purification cycle, as described by Tiefenbach *et. al.*[7], of the precursor was undertaken after the Pyrex tube was mounted.

4.2.1 Parameter

My MBE systems allows to vary growth conditions by changing the substrate temperature, the effusion cell temperature, and the precursor influx via the dosage valve. Diagnostic methods, accessible to me to monitor the growth process, are the chamber pressure, the sample temperature measured by a pyrometer, and the effusion cell temperature measured with a k-type thermocouple.

For the conducted growth processes, the precursor influx was regulated by the dosage valve and was kept constant during all growth processes. Due to the lack of a residual gas analyzer in my system, I was not able to accurately determine the $W(CO)_6$ partial pressure. However, I approximated the introduced amount of $W(CO)_6$ by recording the chamber pressure before and after the leak valve was opened as $6(2) \times 10^{-7}\,\mathrm{mbar}$ before growth and $1.8(2) \times 10^{-6}\,\mathrm{mbar}$ during growth for all reported growths. Furthermore, I continuously monitored the chamber pressure over the growth duration to ensure that the precursor influx stayed constant.

The desirable process parameter to know from the Te effusion cell would be the incoming Te flux on the sample. Because of the lack of a quartz crystal monitor (QCM) in my chamber, this parameter is not accessible to me. However, the Te effusion cell flux is monotonically increasing with temperature[63]. Furthermore, I observed a constant receptacle filling level for all growths, suggesting no changes of Te flux due to decreasing material availability. Therefore, I assume that I reliably reproduced the Te flux for the different growths by setting the effusion cell temperature to the same value.

With the pyrometer I continuously monitored the sample temperature during the growth. Due to a lack of view port shutters, the view port — through which the pyrometer was pointing at the sample — got coated with Te over time. This effect was

visible by eye because the reflectivity of the view port increased consecutively with every growth. It was also frequently observed for growths series two that the sample temperature decreased by a few degrees at a constant heating current over the growth duration of $3\,\mathrm{h}$. I could not elaborate to which extend this was caused by the view port getting coated or because the systems becomes slightly more conducting and therefore reduces its heating power at constant heating current. Due to the small temperature change during one growth I don't expect the effect to significantly bias my results. However I cannot fully rule out a systematical underestimation of the substrate temperature which would accumulate for subsequent growths. Assuming a temperature decrease of $3\,^{\circ}\mathrm{C}$ to $5\,^{\circ}\mathrm{C}$ per growth I would end up with an offset of $30\,^{\circ}\mathrm{C}$ to $50\,^{\circ}\mathrm{C}$ after my entire growth study. But taking into account that the Te effusion cell flux was higher for the second growth series, I can assume that the effect, if apparent at all, will even be less pronounced for the first growth series.

4.2.2 Preparation

sample preparation before every growth consisted of cleaving the sample in air and mounting it to the sample holder. I visually inspected every cleave under the microscope and repeated if the result was not satisfactory. A cleave was considered successful when no flaked-off surface layers were present and a large, macroscopic terrace structure was visible. I mounted the HOPG sample after cleaving on the sample holder (see Fig. 4.2 for an example of a mounted sample). As described above, I placed a SiC plate between the bridge parts and the HOPGsample to increase the heating efficiency. After installation, I measured the resistivity between the spring clamps, bridge parts, and the sample holder base plate to ensure reproducible clamping conditions. Particularly, that means I checked that the base plate is electrically isolated from the spring clamps and bridge parts; the resistivity between spring clamp and bridge parts is larger than between the two bridge parts (i.e. ensure that the current flows through the SiC); and that the resistivity between spring clamps was as low as expected for HOPG (i.e. ensure that sample clamps on both sides of the HOPG properly).

4.2.3 Procedure

The growth process can be divided into three main steps: pre-annealing, film growth and post-annealing. The pre-annealing of the HOPG substrate is necessary to remove

carbon and hydrogen functional groups from the surface[85]. In the literature, pre-annealing temperatures vary from $500\,^{\circ}\mathrm{C}$ to $800\,^{\circ}\mathrm{C}$[6,47,85,86]. For my first growth series I used pre-annealing temperatures ranging from $550\,^{\circ}\mathrm{C}$ to $750\,^{\circ}\mathrm{C}$ were for the second growth series I set it to $800\,^{\circ}\mathrm{C}$. I argue that such a high pre-annealing temperature is beneficial because Kwon *et. al.* [85] showed that CO compounds can be chemisorbed at HOPG up to $1000\,^{\circ}\mathrm{C}$. To start the growth, the Te effusion cell was first ramped up to . $275\,^{\circ}\mathrm{C}$ or $325\,^{\circ}\mathrm{C}$. After stabilizing the effusion cell temperature at its operation temperature for $15\,\mathrm{min}$, the precursor dosage valve was opened. The growth time refers to the time between opening and closing the dosage valve since these two events mark the beginning and end of the deposition process. The growth duration was $3\,\mathrm{h}$ for all grown samples.

After the growth was finished, the sample was post annealed at the process temperature for $30\,\mathrm{min}$ with the Te effusion cell turned off. Right after the growths finished, were the samples transferred to the XPS measurement systems. The air-exposure time during the transfer was kept below $8\,\mathrm{min}$ for all samples. Subsequent to XPS, I measured first SEM and after that AFM.

5 Results

5.1 Film Composition

I employ x-ray photoelectron spectroscopy (XPS) to characterize the coverage and composition evolution under varying growth parameter. To do this I focus on the the $4f$ and $3d$ core level peaks of tungsten and tellurium. I further perform the XPS measurement on a grid of measurement points to account for spatial inhomogeneities resulting from my growth setup.

The W *4f* peak has two spin-orbit components, $4f_{7/2}$ and $4f_{5/2}$, with a splitting of $\Delta = 2.18\,\mathrm{eV}$, whereas the peak $4f_{7/2}$ is located at $31.3\,\mathrm{eV}$ and has a full width at half maxium (FWHM) of $0.3\,\mathrm{eV}$[87,88]. Oxidation of tungsten to WO_3 — where tungsten is in the (VI) oxidation state — leads to a peak shift of the $4f_{7/2}$ to $35.8\,\mathrm{eV}$[88,89]. I will later quantify the ratio of these two peaks to estimate the degree of oxidation. The WO_3 oxide peaks overlay with the much broader $W5d_{3/2}$ peak as exemplified in Fig. 5.1[90]. Because the difference in cross section between the W *4f* and the $W5d_{3/2}$ is around than order of magnitude[91] at my photon energies and since the sensitivity of my analysis is smaller than this contribution I will not consider it in my fitting routine. Furthermore, the W-Te bond leads to a peak shift of the W *4f* level by $\Delta \approx 0.5\,\mathrm{eV}$ — providing the possibility to distinguish WTe_2 from elemental tungsten. However this can be ambiguous if carbon is involved because the W-C bond leads to a peak shift with comparable binding energies[90].

The Te and TeO_2 $3d_{5/2}$ peaks are located at $573.5\,\mathrm{eV}$ and $576.8\,\mathrm{eV}$ respectively, with a peak width of $1.55\,\mathrm{eV}$[92]. The spin-orbit split Te $3d_{3/2}$ is shifted by $\Delta = 10.4\,\mathrm{eV}$[93]. Besides the Te *3d* peaks there are also the Te *4d* peaks detectable, which have the benefit of being in the same binding energy range as the W *4f* peaks (see Fig. 5.1). However, due to the low $4d$ core-level cross section of Te in the photon energy range of the XPS system and the low coverage, I do not get a good enough signal-to-noise ratio and will therefore mainly focus on the Te *3d* levels.

As mentioned above, to account for spatial inhomogeneous film-growth dynamics I recorded XPS spectra on a $4\,\mathrm{mm} \times 6\,\mathrm{mm}$ grid spanning the majority of the sample. Fig. 5.2 shows a compilation of all XPS spectra recorded on one sample. The plot

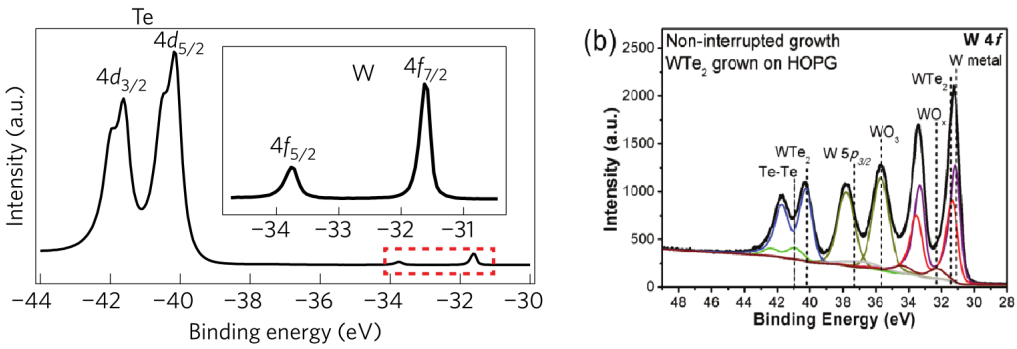

Fig. 5.1: XPS spectra from MBE-grown WTe_2 shows the typical Te *4d* and W *4f* peaks structure. The different intensity ratio between the peaks from a and b is due to the use of different photon energies in the two experiments. The high WO_3 concentration in b is because the sample was exposed to air before the measurement. Figures are adapted from[30] and[90].

is arranged in a way to emphasize the respective location of the displayed plots across the sample. It is visible that the peak intensities vary heavily across the sample. The distribution of peak intensities in x and y direction follows a common pattern across the various samples. Along the x direction, the pattern does not change qualitatively. In y direction the sample can be subdivided in three different regions with respect to the prevailing peak intensity: the outermost regions, shaded in grey, ($y < 1.0\,\mathrm{mm}$ and $y > 5.0\,\mathrm{mm}$) show nearly no signs of XPS core level peaks implying no film coverage. This is expected because this sample region is covered by the sample clamps during the growth (Fig. 4.2 c); The second region, shaded in blue, ($1.0 < y < 2.0\,\mathrm{mm}$ and $4.0 < y < 5.0\,\mathrm{mm}$) accommodates the highest peaks intensities across the sample as can be seen in Fig. 5.2. Whereas the third region, shaded in orange, ($2.0 < y < 4.0\,\mathrm{mm}$) — spanning the middle part of the sample — has the most homogeneous peak intensity distribution. The cause for the strong intensity differences between region two and three will be discussed in chapter 6. In my further analysis I will focus on region three, which is the most homogeneous among the three regions, and therefore resembles best the process-parameter-dependent growth dynamics.

By fitting the XPS spectra, I quantify the core level peak position and area which allows me to deduce the substrate coverage and chemical composition — especially the degree of oxidation and the W-Te ratio. I used a Shirley function to subtract the background and a Gaussian form to fit the peaks. A Gaussian function is only an approximation for the asymmetrically shaped metallic peaks like tungsten[87], However, I expect the error to be negligible compared to the spatial peak variations I observed within the region of interest

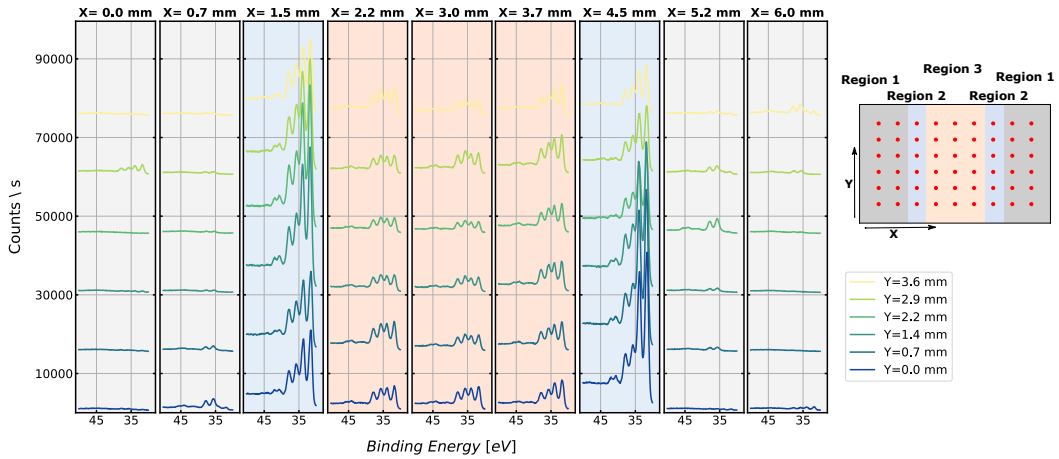

Fig. 5.2: covering an area with XPS measurements allows to distinguish three different growth regions across the sample: minimal growth at the edges (region one), maximal growth (region two) and pristine growth with a homogeneous coverage in the middle of the sample (region three). Inset on the right side shows the sample with the XPS measurement grid indicated by the red dots. The regions one,two and three, are indicated by the different colored shades : one corresponds to grey, two is light blue and three is orange.

A typical fit to the spectrum is shown in Fig. 5.4. The light-blue curve at the upper part of the graph shows the difference between fit and measurement. The ripples around the W *4f* peaks occur for all fit spectra where the W-peak intensity is well above the noise floor. I consider two possibilities for this feature: (1) the Gaussian fit does not resemble the asymmetric W-peak shape well enough or (2) the W *4f* contains a contribution from another compound (e.g. WTe_2 or WC) However, from this it is possible to estimate an upper limit for the inaccuracy introduced by my choice of Gaussian functions for fitting the W-peaks. Comparing the area under the ripples with the standard deviation on the mean peak area values in Fig. 5.5, it is fair to say that my choice of Gaussian functions does not introduce a significant inaccuracy.

To be able to compare the measured intensities across various samples I have to calibrate my measured spectra. This is done by using the predominant C *1s* feature coming from the HOPG surface. On every sample I recorded a survey scan spanning the energy range of all XPS features I am studying. By this I can verify that the C *1s* peak intensity is not significantly compromised by the grown film. This is a reasonable assumption considering the large difference between the detected spectral weight from the C *1s* core levels compared to all the other recorded signals combined — given that all relevant cross sections are in the same order of magnitude for the used photon energy[91]. The calibration curve is obtained by normalizing the C *1s* peak height (grey dashed line in Fig. 5.3 b).

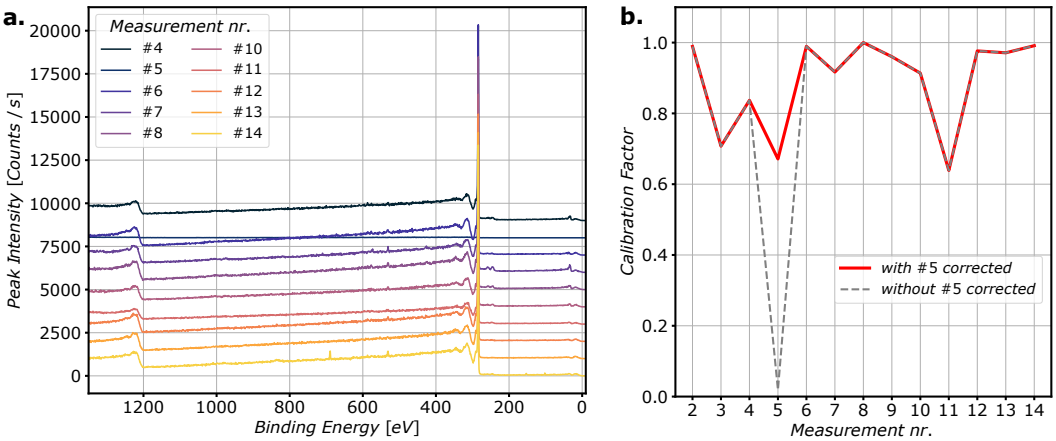

Fig. 5.3: **a** shows the uncalibrated survey spectra for all measured samples. It is visible that the dominant feature is the C *1s* peak. **b** The red curve illustrates the calibration factors I applied to my data. It is extracted from the C *1s* peak height of the survey spectra displayed in a. combined with a correction factor for #5. The dashed grey curve illustrates the calibration factors without #5 being corrected.

The effective calibration curve I used, is illustrated in Fig. 5.3 b in red. It is obtained by normalizing the C *1s* peak heights for every survey spectrum (grey dashed line in subplot b.) whereas I introduced a correction factor for the calibration factor for sample #5. The low intensity measured in the survey spectrum for #5 presents an outlier in the calibration curve, as also among the other measurement points on sample #5. Comparing the background noise around the W *4f*, Te *4d*, and Te *3d* spectra show that the background noise floor for all other measurement points in sample #5 have values comparable to the survey spectra from the other samples. I therefore conclude that the survey spectrum acquired on #5 for itself is not credible. To correct for this I introduced a scaling factor such that the background noise level of the #5-survey spectrum will show the same intensity as spectra recorded at other locations on #5. The scaling factor was obtained by computing the ratio between the averaged noise level between $48\,\mathrm{eV}$ to $50\,\mathrm{eV}$ for a Te *4d* spectrum and form the survey scan. As stated above, applying the correction factor to the calibration value of from sample #5 leads to the red curve in Fig. 5.3 b which fits well within the intensity fluctuations observed for the other samples.

I applied the above stated methods to a series of samples produced with different growth settings. I conducted two growth series at two different Te effusion cell temperatures ($275\,^{\circ}\mathrm{C}$ and $325\,^{\circ}\mathrm{C}$). In those series I varied the substrate temperature in a range from $475\,^{\circ}\mathrm{C}$ to $700\,^{\circ}\mathrm{C}$. Tracking the peak area over temperature allowed to map out composition and concentration changes which will me allow to draw conclusions on the prevailing growth dynamics. Fig. 5.5 shows the temperature

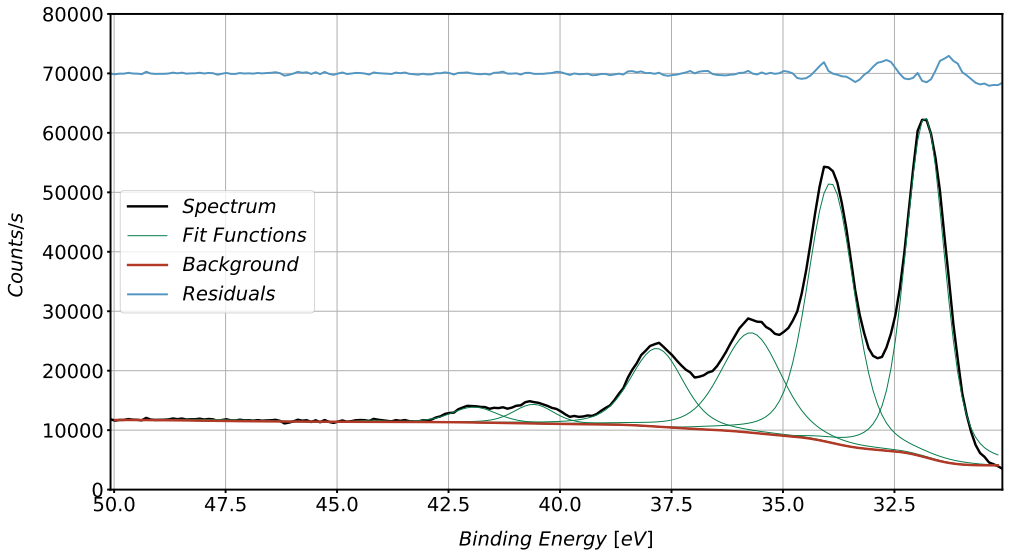

Fig. 5.4: The measured XPS spectrum (black) is fitted — after the background is subtracted (red) — by Gaussian forms (green) to quantify the response from the probed core levels. The difference between measurement and fit is indicated by the blue line. Important point to mention here is that the cut-off for low binding energies is set too high, disregarding the lower tail of the W $4f_{7/2}$ peak. This can be a source of error for the background estimation. However, we assume that this effect will be negligible compared to the large peak intensity fluctuations we encounter (see Fig. 5.5).

dependence of the peak areas - spatially averaged over what I above defined as region three (see Fig. 5.2) — for the W *4f* and Te *3d* and their oxidation states.

Focusing on the first growth series it is visible that the tungsten concentration increases for increasing substrate temperature. This is as expected since the precursor cracking rate is enhanced when more thermal energy is provided. The WO_3 concentration follows the same trend up to $550\,°C$ but has a smaller slope at higher temperatures resulting in a large concentration of non-oxidized tungsten. The Tellurium concentration shows a more complex dependence on sample temperature (Fig. 5.5 b), with a steep increase below $T = 600\,°C$ and a rapid decrease at higher temperatures. The TeO_2 concentration on the contrary seems to stay rather constant above $550\,°C$. The overall incorporated tellurium concentration (indicated in black) is approaching the TeO_2 concentration for increasing temperatures, showing the disappearance of non-oxidized Te above this temperatures.

Comparing the results from series one and series two I find qualitative similarities: the higher WO_3 concentration which prevails in series one at temperatures below $575\,°C$ is also present in the series two at the same temperatures. The peak intensity for W and WO_3 is similar for both Tellurium fluxes. On the other hand, at an increased Te flux, the onset of the Te peak seems to be hindered or moved to higher temperatures outside the investigated temperature range. This is in agreement

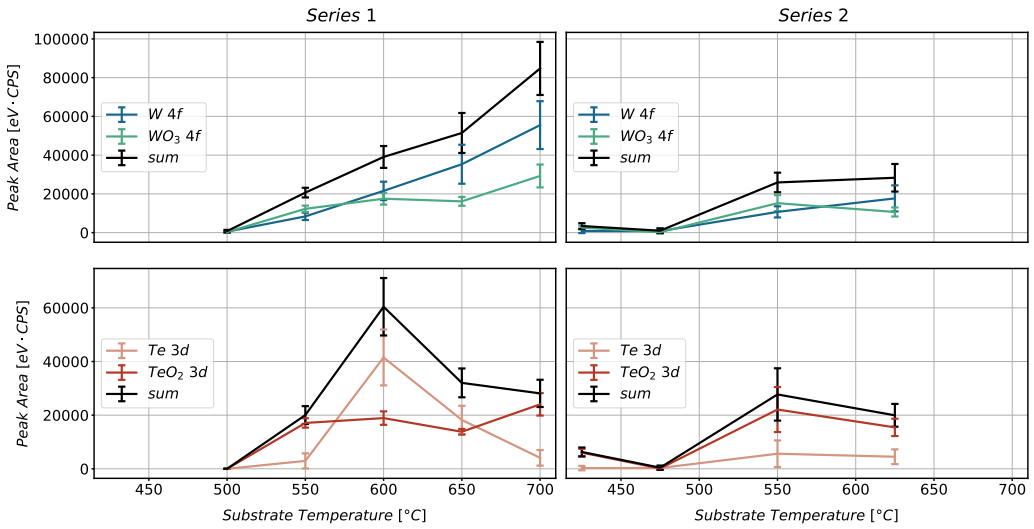

Fig. 5.5: Peak area mean values averaged over growth region three. **a** and b reveal an intermediate temperature range in which the W and Te concentration exceed their oxidized counterparts for growth series one. The large error bars are due to XPS peak intensity fluctuations across region one of the sample.

with an observation in the HOPG/WS_2-system by Tiefenbach et. al. that shows that elevated chalcogenide concentrations during growth can have an inhibiting effect on the growth rate[7].

5.2 Film Morphology

To study the growth dynamics on a microscopic scale and its implications on the film morphology, I employ surface-imaging techniques like SEM and AFM. I systematically recorded SEM images on a mesh spanning across the sample to correlate the local morphology with the spatial-coverage information obtained by XPS. AFM was then used to retrieve the height information of the observed structures and to measure shallow features which cannot be resolved clearly by SEM.

Similar to my XPS data, the SEM images of the sample morphology suggest a subdivision into three regions, as illustrated in Fig. 5.6 and Fig. 5.7. For region three, the film morphology is illustrated by images from two different length scales. Fig. 5.6 a-d refers to a field of view of about $10\,\mu\mathrm{m}$ and Fig. 5.6 e-h shows a field of view around $1\,\mu\mathrm{m}$. The prevailing features in this region are bright, one-dimensional lines which contrast noticeable from the darker HOPG surface. These one-dimensional structures are several nanometers high and are mostly located at the step edges of the HOPG substrate, as measured in the AFM topographies and linecuts presented

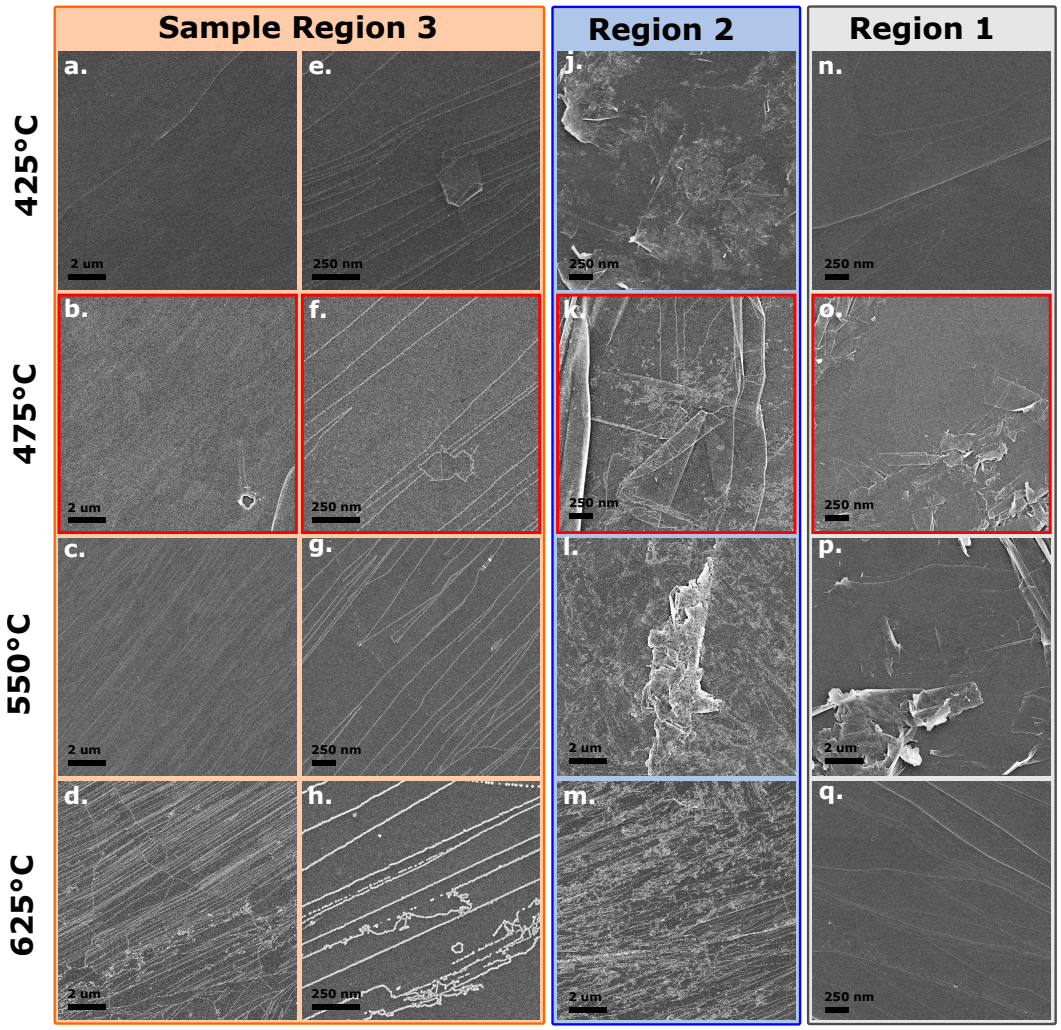

Fig. 5.6: SEM images of the samples at various growth temperatures of series two. The samples are subdivided into similar measurement regions as introduced for the XPS measurements (see inset of Fig. 5.5). The film morphology varies qualitatively for the different regions and is consistent over varying substrate temperatures. The SEM images (b,f,k,o) from the sample grown at 475 K, framed in red, show the same film morphologies as seen on the other samples. However they are located differently across the sample and do not match the classification scheme introduced for the XPS measurements as can be seen in Fig. 6.2 a-l.

in Fig. 5.8. Comparing region one to region three (Fig. 5.6 n-q and a-h respectively), I see that the bright one-dimensional features only appear in region three, where I— based on the XPS data — expect film coverage. I therefore conclude that the one-dimensional structures are the grown film. This is in agreement with reported growths of various metals (e.g. Mo, Pd) on HOPG substrates by Electrodeposition — resulting in similar one-dimensional structures along step edges[94–96]. This allows

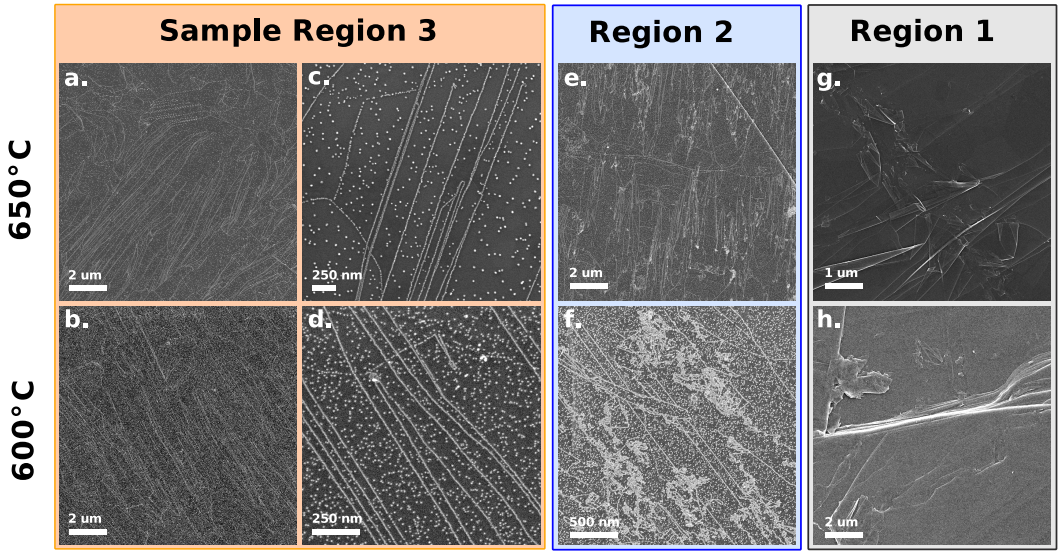

Fig. 5.7: **a** to **f** SEM images of samples grown at 600 °C and 650 °C from the first growth series illustrate the highest coverage observed in this growth study. This agrees with my XPS measurements (Fig. 5.5 where the largest W and Te peak intensities were measured at these two substrate temperatures. The samples are again subdivided into measurement regions one to three as introduced for the XPS measurements (see inset in Fig. 5.5). **g** and **h** SEM images recorded at region one show the bare HOPG substrate as expected.

me now to relate the temperature-dependent W-concentration decrease (Fig. 5.5) with the fading SEM intensity in Fig. 5.6 f to h; and with the height decrease of the one-dimensional structure recorded in AFM (Fig. 5.8 a to c).

Region two shows a less homogeneous film morphology, in agreement with the larger XPS-peak-height variations. The film morphology varies qualitatively between ordered structures (not shown) which are similar to the ones observed in region three, and more irregular, curly patterns (Fig. 5.6 j-m). This is in agreement with my observation of irregularly high XPS peak intensities at single, randomly distributed spots inside region two (see Fig. 5.2). I distinguish this curly film morphology qualitatively from the film morphology of region three.

In region one, most areas show little to no coverage. This is illustrated by comparing Fig. 5.6 n-q form region one to Fig. 5.6 j-m from region two. Topographical features from the substrate like flaked off HOPG patches (Fig. 5.6 l,o,p) and step edges (Fig. 5.6 m,n,q) are present in both regions. It can be seen that region one shows no accumulation of one-dimensional structures at the topographical features of the substrate.

The higher XPS peak intensities (Fig. 5.5) from the samples with substrate temperature 600 °C and 650 °C from series one are accompanied by the appearance of a new film-morphological feature: a high-density dot-like pattern on the HOPG terraces as

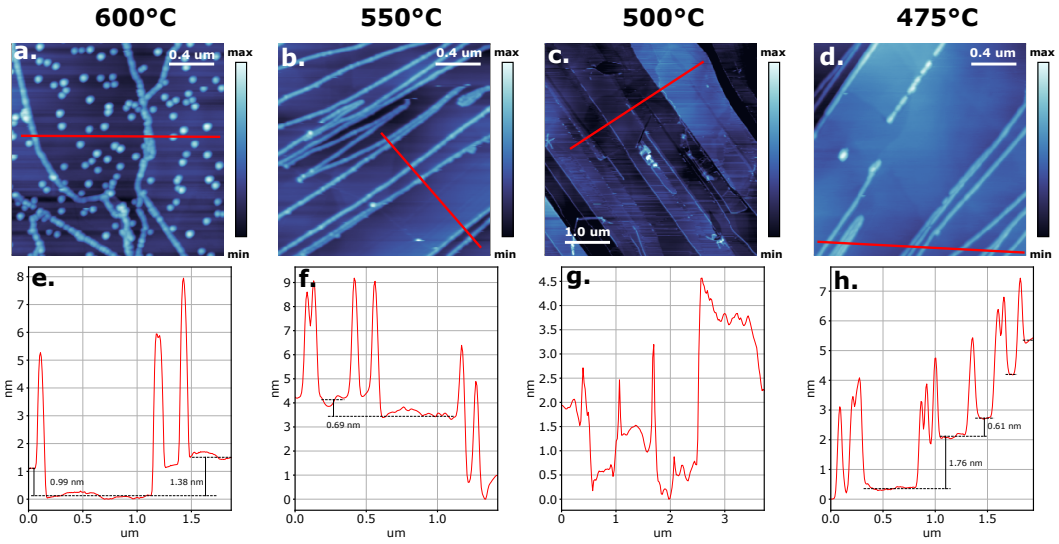

Fig. 5.8: **a-c** and **e-g** are AFM topographies from sample of growth series one, whereas **d** and **h** are from series two. The HOPG-substrate step edges are visible in all linecut plots (a-d). In subplot a, b, and d I estimated the step edge height to confirm that they are integer multiples of a graphite monolayer ($0.33\,\mathrm{nm}$)[97].

visible in the SEM images in Fig. 5.7 a-f. These dots have a lateral expansion of a couple of nm (Fig. 5.7 c and d). The dot height is similar to the one-dimensional line structure at the step edges (Fig. 5.8 a and e). This is somewhat surprising, because from the fact that these high-density dot patterns only appear above a certain temperature — corresponding to a certain sample coverage — one could expect that the dot formation is followed by a preceding saturation of the nucleation sites on the step edges. The observation that both structures — dots and lines — show the same height, however, rather supports the assumption that both features start to develop at the same time at the beginning of the growth process. This could be investigated in the future by conducting a study varying the deposition time to get a better understanding of the formation of the different structures. Furthermore, such dot pattern can also be found on isolated locations on the $625\,^{\circ}\mathrm{C}$ sample of growth series two but with a much lower density (not shown). In that sense it is interesting to see, that an increase in chalcogene flux for constant substrate temperatures (compare Fig. 5.7 c-d with Fig. 5.6 h) causes such a drastic change in surface morphology by inhibiting the formation of this dotted patterns.

The film morphology in growth region 2 Fig. 5.6 — with its curly unordered structure — shows significant differences compared to the one-dimensional and dotted structure shown above. These patches consisting of curled and ramified branches can be seen as a reason for the drastically increased peak intensity in the XPS spectra of region 2.

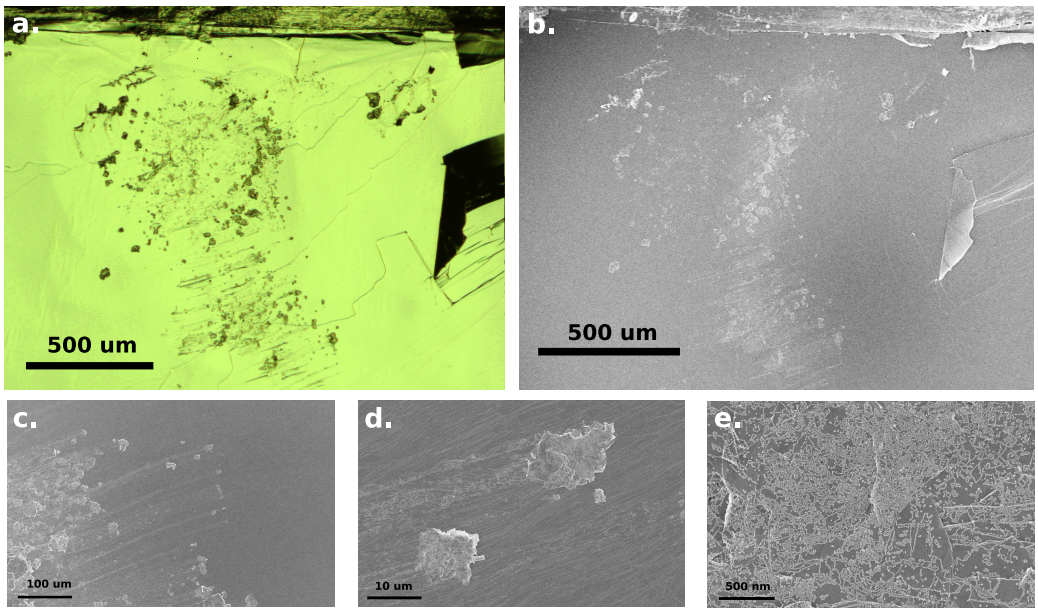

Fig. 5.9: **a** optical image showing scratches on the surface of the HOPG substrate. **b-e** SEM image of the same location at magnifications from 100x up to 100000x. By comparing the optial and SEM image it is possible to link the observed curled structure to macroscopic mechanical defects of the HOPG surface.

A reason for this dendritic features is illustrated in Fig. 5.9. The image shows optical (a) and SEM images (b-e) of the same sample location. The scratches and dents on the HOPG surface can clearly be seen in the optical image as dark streaks and spots. The dark spots are sheared off flakes — recognizable in panel d. In panel b and c it is visible that the dark streaks from panel a appear as brighter features in the SEM images. Zooming in — as illustrated in panel e — reveals their dendritic structures which is similar to the one observed in Fig. 5.6 j-m and Fig. 5.7 e-f.

6 Discussion

6.1 Film Composition

My XPS results indicate a pronounced temperature dependence of the film composition and precursor dynamics, which I put into context to existing literature. My measurements (Fig. 5.5 a) reveal an increase of tungsten and tungsten oxide for increasing substrate temperatures. A similar trend has been reported for $W(CO)_6$-based metal-organic growth of WS_2 by Tiefenbach *et. al.* [7,98]. The authors argue that such a behavior indicates that the kinetic activation of the reaction – i.e. breaking off the CO ligands from $W(CO)_6$ — is the growth limiting parameter. This interpretation agrees with my data as can be seen in the monotonic increase of the W concentration for increasing temperatures in Fig. 5.5 a.

I determine now the stoichiometry of the film from my XPS measurements. I will focus on the film grown at $600\,^{\circ}\mathrm{C}$ from series one since it has the highest Te concentration (Fig. 5.5 a,b). The averaged peak area values from sample region three for the W *4f* and Te *3d* core level peaks are $A_{\mathrm{W},4f} = 2.15 \times 10^4$ CPS $\cdot$ eV and $A_{\mathrm{Te},3d} = 4.10 \times 10^4$ CPS $\cdot$ eV. The Te $3d_{5/2}$ and Te $3d_{3/2}$ electrons have a kinetic energy of $913\,\mathrm{eV}$ and $903\,\mathrm{eV}$ when leaving the sample which corresponds to an inelastic mean free path of $\lambda_{\mathrm{Te},3d} = 20.5\,\text{Å}$, whereas the W $4f_{7/2}$ and W $4f_{5/2}$ electrons have a kinetic energy of $1455\,\mathrm{eV}$ and $1453\,\mathrm{eV}$ resulting in $\lambda_{\mathrm{W},4f} = 17.6\,\text{Å}$ [100]. For the photoionization cross section, I used $\sigma_{\mathrm{W},4f} = 0.15\,\mathrm{Mb}$ and $\sigma_{\mathrm{Te},3d} = 0.42\,\mathrm{Mb}$ given a photon energy of $\hbar\omega = 1486.6\,\mathrm{eV}$ [101]. The asymmetry parameter β at our photon energy is given as $\beta_{\mathrm{Te},d3} \approx 1.17$ and $\beta_{\mathrm{W},4f} = 1.03$ [102]. Employing eq. 3.5 with the values from above we get

$$c_{\mathrm{Te}}/c_{\mathrm{W}} = \frac{A_{\mathrm{Te},3d}\,\sigma_{\mathrm{W},4f}\,\lambda_{\mathrm{W},4f}\beta_{\mathrm{w},4f}}{A_{\mathrm{W},4f}\,\sigma_{\mathrm{Te},3d}\,\lambda_{\mathrm{Te},3d}\beta_{\mathrm{Te},3d}} = 0.57 \tag{6.1}$$

A ratio of $1:2$ for W:Te would indicate perfectly stoichiometric WTe_2, whereas my results indicates a Te deficiency in the grown structure. In MBE processes which provide W by electron-beam evaporation, the transition metal excess is normally explained by either the lower sticking coefficient of the Te, or by the fact that the Te

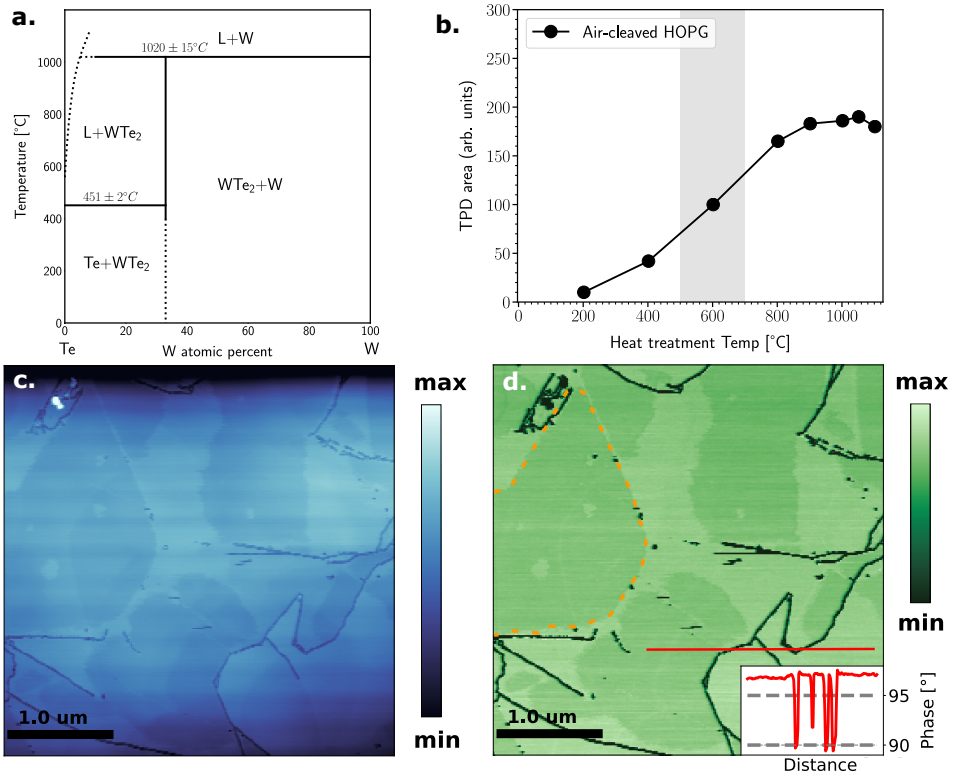

Fig. 6.1: **a** The Te-W phase diagram shows WTe_2 as the only stable compound formed by W and Te, present in different phases with either an excess in Te or W. Adapted from 99. **b** Temperature-programmed desorption (TPD) measurement of an HOPG surface is drawn here to illustrate the desorption behavior of CO molecules. The shaded area highlights the temperature range with an increased CO-desorption rate. Adapted from 85. c and **d** Height and phase image of an AFM measurement on a sample grown at $475\,^{\circ}\mathrm{C}$ substrate temperature from growth series two. The good correlation between the dark patches is visible in both images and is an indication that the patches are composed of a different material than the HOPG substrate. For clarity of of the dark patches in d is bordered by an orange dashed line. The horizontally stripes in the topography are measurement artifacts as a result of instabilities during the scan due to the equipment we used. The inset in d shows the cross section taken along the straight red line on the phase image that is shown in d. From this it is visible that the phase can drop below $90\,\mathrm{degree}$ at the dark one-dimensional structures, which indicates that the measurement is performed close to the transition to the repulsive regime and therefore sensitive to compositional changes.

flux from conventional effusion cells consists of a range of Te_n clusters ($n = 1 - 8$) with larger dissociation energies, hindering the incorporation of Te into the film[90].

My growth-temperature-dependent XPS measurements further suggest that the grown films contain WTe_2. Taking into account that: Te, with its high vapor pressure, gets incorporated into the film at substrate temperatures up to $700\,^{\circ}\mathrm{C}$; and Te can be clearly distinguished from its oxidized counterpart; I suspect that Te has to undergo a bond with the W atom[†]. Focusing on the Te-W phase diagram (Fig. 6.1 a) I see that

[†]I didn't find any publications describing Te-C as a stable chemical compound which led me to the assumption that Te-C is unlikely to form in my deposition process.

the Te-deficiency corresponds to a phase where WTe_2 and elemental W coexist. Since there doesn't exist another stable phase with a different stoichiometry for Te and W, I conclude that WTe_2 forms on my sample. I furthermore rule out the formation of an amorphous W-Te phase given the slow growth rates where the one dimensional structures at the step edges — showing a maximal height of $8\,\mathrm{nm}$ (Fig. 5.8 e-h) — develop over a deposition time of $3\,\mathrm{h}$.

Considering the different crystal-structure properties of the elemental W and WTe_2 phases I hypothesize that they condense at different topographical features on the HOPG substrate (i.e at the step edges or across the terraces). The three-dimensional Vollmer-Weber growth mode[63], present at the HOPG step edges, requires strong out-of-plane bonds within the deposited nanostructure, compared to bonds between the nanostructure and the substrate. From this observation I conclude that the two-dimensional vdW material WTe_2 is unlikely to form such a three-dimensional film morphology on the HOPG step edges. I therefore assume that these three-dimensional structures consist mostly of elemental tungsten.

An interesting case presents the sample with substrate temperature $475\,\mathrm{K}$ from series two because its AFM measurements show patches of uniform height and strong contrast in the phase image as presented in Fig. 6.1 d. In general, phase contrast in AFM tapping-mode measurements, if it is not a measurement artifact, is caused by differences in surface properties (e.g. roughness, chemical composition, flaked-off substrate layers) which lead to a changes in the tip-surface coupling[80,81]. This aligns well with our hypothesis presented before. The good correlation between these patches in the height image (Fig. 6.1 c) and phase image (Fig. 6.1 d) is a strong indication that this is not a measurement artifact but rather a change of surface properties. I performed this measurement in the attractive regime close to the transition point to the repulsive regime (Fig. 3.3 b) visible in the phase values which are above $90°$ but decrease when the tip is moving along the one-dimensional nanostructures (see inset of Fig. 6.1 d). This mode of operation (i.e. in the attractive regime close to the transition) is favorable to observe contrast effects on the surface which would explain why such phase-contrast patches were seen on other samples (Fig. 5.8)[103]. Furthermore, due to the unstable measurement condition these measurements do not provide reliable height information as can be seen in the height image: the one-dimensional structures at the step edges in Fig. 6.1 c (dark lines), have a lower height than the terraces which is artificial since it contradicts other AFM images from the same and other samples (Fig. 5.8 e-h). This error in the height image also explains why these patches are dark, i.e. at lower heights than the surrounding HOPG, which is in contrast to our expectation that they are films on top of the HOPG surface. Considering these arguments, we

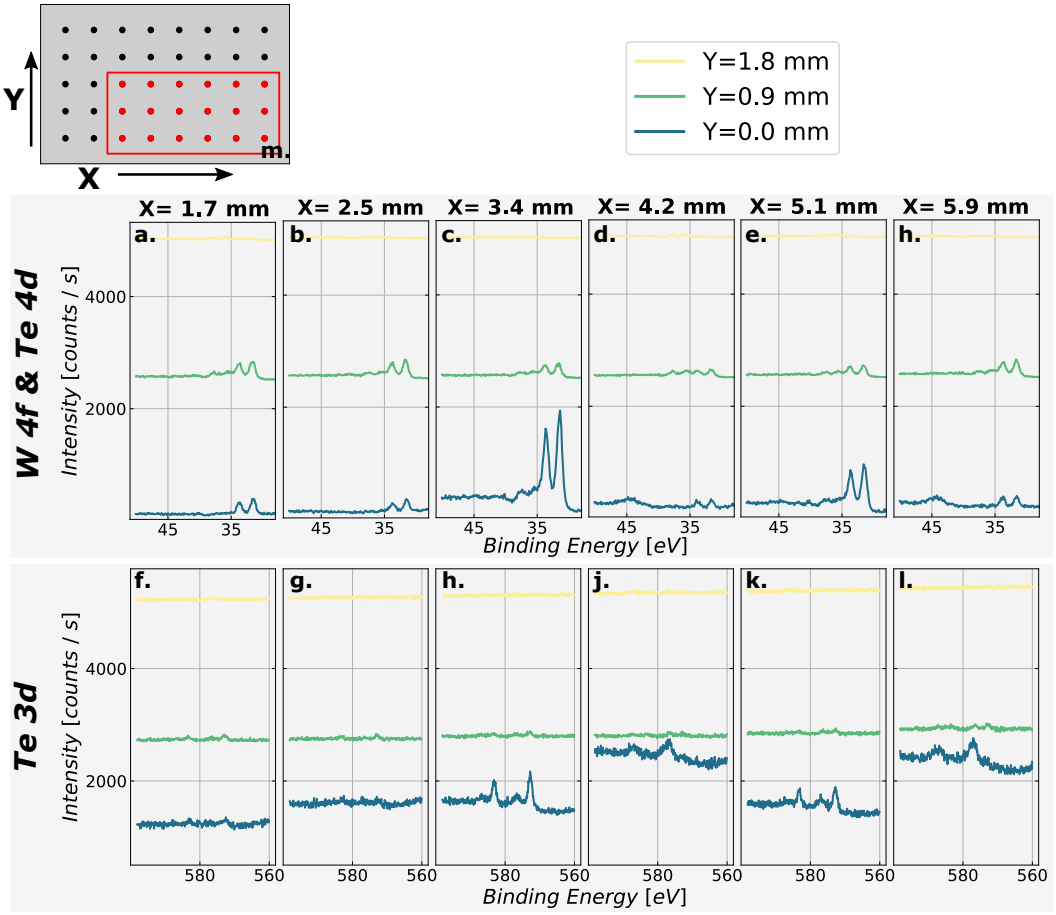

Fig. 6.2: **a-l** XPS spectra of the W *4f* (a-h) and the Te *3d*(f-l) core level peaks measured across a selected region (red dots in m) of the sample from series two with growth temperature $475\,\mathrm{K}$. **m** Red dots indicate the location of the displayed XPS spectra on the sample (dark grey box).

interpret the increase in contrast in the phase image as an indication for a chemically different layer present on the HOPG surface, supporting our hypothesis that thin film WTe_2 forms on the HOPG terraces. However, to confidently say that the observed patches are stoichiometric WTe_2 thin-films further investigations for example by atomic resolution STM or AFM are required.

The sample of series two, grown at $475\,\mathrm{K}$, represents a special case compared to the other samples because its XPS measurement does not match with the characterization scheme we introduced in chapter 5. The spatial XPS peak height variations (Fig. 6.2 a-l) do not allow to subdivide the sample into region one, two, and three. Instead it shows significantly lower average peak area compared to the other grown samples (Fig. 5.5) and the substrate coverage occurs predominantly along the lower edge of the sample ($Y = 0\,\mathrm{mm}$) with single spots of increased peak intensities (e.g. $X = 3.4\,\mathrm{mm}$ and $X = 5.1\,\mathrm{mm}$ at $Y = 0\,\mathrm{mm}$). The left region and the upper half

of this sample, indicated as black dots in Fig. 6.2 m, show no XPS peak intensities and are therefore not plotted in Fig. 6.2. From the good agreement of the spatial XPS peak height distribution across the other samples from series one and two, I conclude that the irregularities seen here are due to external factors like improper clamping of the sample. Nevertheless this sample constitutes an interesting case since it directly shows the coexistence of two different growth morphologies, i.e. one-dimensional nanostructures at the step edges (Fig. 5.6 f,k and Fig. 5.8 d) and two-dimensional patches (Fig. 6.1 c,d).

6.2 Film Oxidation

My XPS results reveal a pronounced oxidation of my films, in form of WO_3 and TeO_2. Here I consider two main sources for the incorporated oxygen: (1) Disintegration of the $W(CO)_6$ molecule provides elemental oxygen during the growth process; and (2) air exposure of the samples between growth and XPS characterization leads to oxidation of the as-grown films. In the following paragraphs, I will present arguments to weight the possibility of either of the two cases.

A strong argument against hypothesis (1) is presented by Tiefenbach[7]: He presents in-situ XPS studies of as-grown pure tungsten and WS_2 films on HOPG and $MoTe_2$ substrates in the temperature range from $450\,^{\circ}\mathrm{C}$ to $550\,^{\circ}\mathrm{C}$; and on sputtered steel surfaces in a temperature range from $250\,^{\circ}\mathrm{C}$ to $550\,^{\circ}\mathrm{C}$. Besides a small peak shift ($\approx 0.5\,\mathrm{eV}$) of the W $4f_{7/2}$ core level at $250\,^{\circ}\mathrm{C}$ substrate temperature, are no signs of oxidation of the W *4f* peaks visible.

These clear results from Tiefenbach[7] are surprising considering various other studies about $W(CO)_6$-based growth processes for pure tungsten films on Ni(100) and W(110)[104–106]. These studies have shown the formation of WO_3 across an intermediate temperature range. A detailed investigation into the chemisorption process of $W(CO)_6$ on Ni(100) surfaces by Zaera *et. al* revealed three different stages of adsorption[105]: (1) around a substrate temperature of $-25\,^{\circ}\mathrm{C}$ all metal bonds from $W(CO)_6$ break to yield CO and W chemisorbed to the substrate; (2) above $125\,^{\circ}\mathrm{C}$ the desorption of CO molecules begins along with the C-O scission leading to the oxidation of the adsorbed W; (3) Around $325\,^{\circ}\mathrm{C}$ to $425\,^{\circ}\mathrm{C}$ the atomic C and O recombine and desorb while W is reduced to its zero valence state leading to oxigen-free W films. The reason for the rather low temperature for complete decarbonylation of $W(CO)_6$ on Ni(100) surfaces is attributed to a charge transfer taking place between substrate and the abdsorbed $W(CO)_6$[105,106].

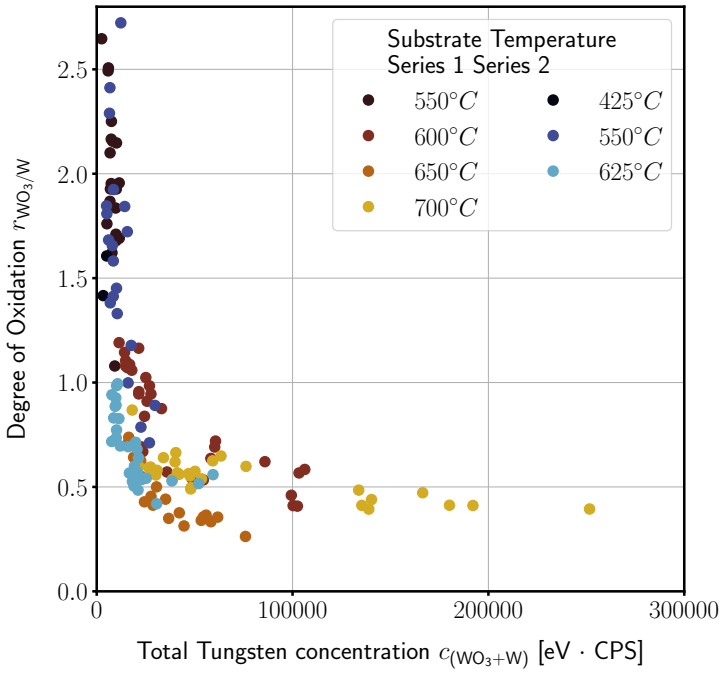

Fig. 6.3: The increased degree of oxidation for decreasing total tungsten volume is a strong indication for surface oxidation of the film. Colored dots represent the degree of oxidation correlated with the W concentration for the XPS measurements conducted in the sample region two and three from the various samples from both growth series. The different dot colors refer to the different samples which were distinguished by their corresponding process temperature.

HOPG is different form metallic substrates as it does not allow for spontaneous decarbonylation at ambient temperatures. Instead, the dissimilation of the $W(CO)_6$ precursor happens thermally, as indicated by the high substrate temperatures necessary to initiate the growth process[7]. However, similarities to the results on Ni(100) and W(110) exists in the fact that CO molecules can adsorb to HOPG up to elevated temperatures. Temperature-programmed desorption studies on HOPG-surfaces reveal the presence of carbon and oxygen-based functional groups (e.g. CO) up to temperatures of $1050\,°C$[85]. This behaviour would allow for CO molecules — released by the decarbonylation of $W(CO)_6$ — to be bound to the surface, where they can act as an oxygen source, up to temperatures of $1050\,°C$. A hint for this to occur can be seen in my data: Focusing on Fig. 5.5, it is visible that an inversion of the W and WO_3 concentration takes place around $575\,°C$ for both growth series as also for the Te and TeO_2 concentration of series one (Fig. 5.5.a-c). This qualitative change coincides with the middle of the temperature range where the steepest decrease of adsorbed CO functional-groups (i.e. $500\,°C$ to $700\,°C$) takes place, as depicted in Fig. 6.1 b[85]. This leads to the assumption that the qualitative change in W and WO_3

in my data around $575\,°\mathrm{C}$ is caused by a reduction of the surface adsorption of CO on HOPG.

I will now discuss hypothesis (2) — oxidation introduced due to air exposure. The spread in film coverage across one sample, measured by XPS (see chapter 5), allows me to investigate a large coverage range with only a few samples. In Fig. 6.3 I plot the relative degree of oxidation $r_{\mathrm{WO_3/W}}$ (i.e. the ratio between the peak area of the WO_3 $4f_{7/2}$ and W $4f_{7/2}$ core levels) in respect to $c_{\mathrm{WO_3+W}}$, the total amount of W present on the substrate. An anti-correlation of the degree of oxidation towards higher amounts of W is clearly visible. The oxidation ratio converges to a stationary value of 0.5 for large amounts of W. A good agreement of this tendency is visible across all samples of growth series one. This agrees well with the hypothesis that oxidation only happens at the surface of my grown structures which entails a decrease of the surface-volume ratio for increased volumes. I understand the divergence of the oxidation at low coverage as a sign that the film gets nearly completely oxidized during the transfer time of $8\,\mathrm{min}$ to the XPS system. Whereas the convergence to an oxidation ratio of 0.5 at high coverage, is an effect of the limited probing depth of the XPS measurement.

My findings are consistent with the oxidation behaviour of elemental W and monolayer WTe_2. From SEM and AFM images (see Fig. 5.7a-m and Fig. 5.8a-c) I know that the grown structure varies from $\approx 3\,\mathrm{nm}$ to $8\,\mathrm{nm}$ in height and is extending over multiple nm in lateral size. Experiments on the oxidation behaviour of elemental W exposed to air show an oxidation rate of $\mathrm{nm/h}$[107]. Similar for few-layer WTe_2, studies showed a degradation of the Raman active modes accompanied by oxygen incorporation after a few minutes of air-exposure[4,108]. I therefore see it as plausible that an oxidation rate in the range of $\mathrm{Å/min}$ can lead to the effect displayed in Fig. 6.3 considering that the duration of air exposure of your samples was around $8\,\mathrm{min}$.

7 Conclusion

Monolayer 1T'-WTe_2 is a QSH insulator up to $100\,\mathrm{K}$ [29] and therefore a promising candidate for many spintronic-based applications. As films grown by conventional molecular beam epitaxy are of poor quality and limited to $100\,\mathrm{nm}$ sized islands [30,39,109], alternative growth methods are required. In this thesis, I developed an alternative, precursor-based UHV compatible approach for the growth of monolayer WTe_2. My efforts have been guided by the following questions: (1) Does stoichiometric, monolayer WTe_2 form on the substrate? (2) What is the morphology of the grown WTe_2? (3) Does the deposited WTe_2 resist to incorporate any other reaction products than W from the precursor decomposition? Beyond the scope of this work are questions regarding the crystallographic phase and defect concentration on an atomic level which are discussed in the following chapter.

Due to cleanliness standards required for MBE, which prohibit introducing metal-organic precursor in non-organic MBE systems, I built a new MBE system tailored for the development of metal-organic growth processes. This included to set up a UHV vacuum chamber, to built a precursor inlet system, a chalcogenide effusion cell, and a direct-current heater stage. This phase of the project consumed two thirds of the total time spent. After the system was operational, I conducted systematic growth studies on HOPG substrates by varying Te effusion cell temperature and substrate temperature while keeping the $W(CO)_6$-precursor concentration constant. I performed two growth series (for Te effusion cell temperatures $275\,^\circ\mathrm{C}$ and $325\,^\circ\mathrm{C}$) where I varied the substrate temperatures to study the growth dynamics.

My study – employing XPS, AFM, and SEM — revealed the formation of WTe_x-based nanostructures at the step edges and on the terraces of my HOPG substrate. I achieved a W:Te ratio of $1 : 0.57$ in my films grown with optimized process parameters, as shown by my XPS core-level measurements. I further argued that the deviation from the stoichiometric ratio $1 : 2$ indicates a parallel growth of elemental W in addition to WTe_2, as the W-Te phase diagram contains only W, Te and WTe_2 as thermodynamically stable phases and the formation of Te is excluded due to the high substrate temperatures. Using SEM and AFM, I was able to show the existence of two topographically-distinct growth structures: the elevated, one-dimensional structures along the step edges observed on all samples and the two-dimensional,

few-atomic-layer patches on the HOPG terraces observed on the sample from series two grown at $475\,\mathrm{K}$. I suspect that these two-dimensional patches also form at other growth conditions. However, I didn't succeed to record such structures on other samples, as driving the AFM close to the transition between the attractive and repulsive regime is challenging for samples with higher coverage and more pronounced three-dimensional features. Based on the necessity for strong out-of-plane bonds to grow three-dimensional structures (Vollmer-Weber growth mode) I hypothesized that elemental tungsten forms in sharply one-dimensional structures at the step edges. WTe_2, on the other hand, prefers to grow in islands on the HOPG terraces due to its two-dimensional structure. This assumption is supported by AFM phase-contrast images showing the presence of patches with a different chemical composition. However, this conclusion is not beyond doubt and more evidence needs to be gathered in further studies using structural characterization techniques (see chapter 8).

My XPS studies showed a pronounced oxygen incorporation in form of TeO_2 and WO_3 in the grown structures. In my analysis, I discussed two reasons causing the oxidation: (1) oxygen was provided by the reaction product form the precursor decarbonylation; or (2) air exposure occurred while transferring the sample to the XPS measurement station. Previous studies on the oxidation behaviour of $W(CO)_6$-based growth processes are contradictory: while Tiefenbach *et. al.*[7] reported no oxidation for WS_2 grown on HOPG, other studies showed a clear oxidation of tungsten films grown on metal substrates[104–106]. My XPS measurements however showed a decrease of the WO_3/W ratio for increasing tungsten concentrations suggesting that mainly the surface of the film is oxidized. With this I can conclude that most of the oxygen is from air exposure. However, I cannot rule out the incorporation of small amounts of oxygen during the process.

8 Outlook

8.1 Film Characterization Improvements

The presented characterization of my metal-organic MBE grown films suggest the formation of WTe_2 and elemental W on HOPG. To obtain direct evidence for the correct structural phase of WTe_2, further studies using surface sensitive techniques such as STM and Raman spectroscopy are required. Due to the low substrate coverage, conventional structural characterization tools like x-ray or neutron diffraction are not applicable. Furthermore, I propose the use of capping layers to answer the question whether the incorporated oxygen stems form the process or from air exposure. I will now briefly introduce these techniques:

STM

The distortion of the W atom along the x axis in the 1T'-phase leads to a slight rearrangement of the Te atoms which can be seen by atomic-resolution STM as a stripe order along the y axis. This, together with the characteristic lattice constant, can be resolved by STM and used as an identifying feature of the 1T'-phase of WTe_2 [30,39,109]. The very recently developed capability of an in-situ transfer between the metal-organic MBE and an STM from the Hoffman group via a vacuum suitcase enables to characterize the as-grown films without risking degradation through air exposure.

Raman

Raman spectroscopy is a photon-in photon-out process which probes low-energy excitations like vibrational modes inside a material. Due to the unique symmetry properties of the T_d-WTe_2 crystal structure compared to other 2H-MX_2 structure, its Raman spectrum acts like a fingerprint allowing to detect the T_d-WTe_2 phase [4,46,110]. Furthermore, the space-group evolution of WTe_2 from bulk (C_{2v}) to monolayer (C_{2h}) leads to the disappearance of certain Raman peaks, which allows to experimentally

distinguish between monolayer (1T') and multilayer (T_d) WTe_2 [110,111]. Raman spectroscopy is normally available as an ex-situ measurement technique and care must be taken by characterizing monolayer WTe_2. The air sensitivity of WTe_2 affects the Raman spectrum and leads to the disappearance of certain spectral features within tens of minutes, as it was shown for exfoliated and chemical-vapor-deposition grown samples [4,46].

Capping layer and Ar sputtering

Due to the lack of access to an in-situ XPS system, I'm required to adapt capping methods to shield the as-grown films from air exposure if I want to avoid oxidation during the transfer to ex-situ measurement systems. In my case, Te would be a natural choice for a capping material since it doesn't introduce impurity atoms in my films [112]. Te is in general a good capping layer because under air exposure the self-passivated oxidation behaviour leads to the formation of a protective TeO_2 layer on the surface, hindering the diffusion of further oxygen into the film [92]. After transfer to the XPS system, the capped film can then be analyzed by successively argon sputtering the capped layer to record depth dependent XPS spectra.

As a different approach, the Ar-sputtering can be used directly to remove the upper most layer of the as-grown and air-exposed nanostructures and films as a direct method to verify the presence surface-layer oxidation.

8.2 Growth Process Improvements

Change of Substrate

My current process of surface preparation by cleaving makes it hard to achieve reproducible surface quality on the HOPG substrates. In my studies of growth parameter optimization by means of film coverage maximization this can introduce uncertainty since the nucleation-site density can change from cleave to cleave. Another disadvantage of HOPG is that the surface is arranged as unordered and overlaying patches of graphene or graphite flakes rather than homogeneously distributed step edges. Finally, due to its van der Waals structure, the surface of HOPG easily flakes off under shearing stress. The sample preparation therefore often leads to the damage of parts of the surface resulting in distinctly high film coverage in these areas. I

assume that this effect is the reason for the high peak intensities in region two (see Fig. 5.2)

Using three-dimensional crystal substrates with two-dimensional passivated surfaces like graphitized 6H-SiC(0001) would allow me to have better control over substrate-step-edge quality and spacing by employing polishing and etching procedures while maintaining a graphite surface[113]. Furthermore it would be less prone to surface damages due to scratches from sample mounting as I saw it on HOPG (Fig. 5.9 a-e) and would therefore allow a more accurate evaluation of growth-parameter dependent coverage changes.

Bibliography

[1] Fu, L. & Kane, C. L. Superconducting Proximity Effect and Majorana Fermions at the Surface of a Topological Insulator. *Physical Review Letters* **100**, 096407 (2008). URL https://link.aps.org/doi/10.1103/PhysRevLett.100.096407.

[2] Wang, G. *et al.* Colloquium: Excitons in atomically thin transition metal dichalcogenides. *Reviews of Modern Physics* **90**, 021001 (2018). URL https://link.aps.org/doi/10.1103/RevModPhys.90.021001.

[3] Tsao, J. Y. *Materials Fundamentals of Molecular Beam Epitaxy* (Academic Press, 2012). Google-Books-ID: 1kgfS1JKhi4C.

[4] Naylor, C. H. *et al.* Large-area synthesis of high-quality monolayer 1T'-WTe 2 flakes. *2D Materials* **4**, 021008 (2017). URL http://stacks.iop.org/2053-1583/4/i=2/a=021008.

[5] Walsh, L. A., Addou, R., Wallace, R. M. & Hinkle, C. L. Chapter 22 - Molecular Beam Epitaxy of Transition Metal Dichalcogenides. In *Molecular Beam Epitaxy (Second Edition)* (ed. Henini, M.), 515–531 (Elsevier, 2018). URL http://www.sciencedirect.com/science/article/pii/B9780128121368000244.

[6] Tiefenbacher, S., Sehnert, H., Pettenkofer, C. & Jaegermann, W. Epitaxial films of WS2 by metal organic van der Waals epitaxy (MO-VDWE). *Surface Science* **318**, L1161–L1164 (1994). URL http://www.sciencedirect.com/science/article/pii/003960289490331X.

[7] Tiefenbacher, S. *Metallorganische van der Waals Epitaxie von MX2*. Ph.D. thesis (1998).

[8] Brahlek, M. *et al.* Frontiers in the Growth of Complex Oxide Thin Films: Past, Present, and Future of Hybrid MBE. *Advanced Functional Materials* **28**, 1702772 (2018). URL https://onlinelibrary.wiley.com/doi/abs/10.1002/adfm.201702772.

[9] Jalan, B., Engel-Herbert, R., Cagnon, J. & Stemmer, S. Growth modes in metal-organic molecular beam epitaxy of TiO2 on r-plane sapphire. *Journal*

of Vacuum Science & Technology A: Vacuum, Surfaces, and Films **27**, 230–233 (2009). URL https://avs.scitation.org/doi/10.1116/1.3065713.

[10] Jalan, B., Moetakef, P. & Stemmer, S. Molecular beam epitaxy of SrTiO3 with a growth window. *Applied Physics Letters* **95**, 032906 (2009). URL https://aip.scitation.org/doi/10.1063/1.3184767.

[11] Marshall, P. B., Kim, H., Ahadi, K. & Stemmer, S. Growth of strontium ruthenate films by hybrid molecular beam epitaxy. *APL Materials* **5**, 096101 (2017). URL https://aip.scitation.org/doi/10.1063/1.4998772.

[12] Brahlek, M., Zhang, L., Eaton, C., Zhang, H.-T. & Engel-Herbert, R. Accessing a growth window for SrVO3 thin films. *Applied Physics Letters* **107**, 143108 (2015). URL https://aip.scitation.org/doi/10.1063/1.4932198.

[13] Wang, T., Prakash, A., Warner, E., Gladfelter, W. L. & Jalan, B. Molecular beam epitaxy growth of SnO2 using a tin chemical precursor. *Journal of Vacuum Science & Technology A: Vacuum, Surfaces, and Films* **33**, 020606 (2015). URL https://avs.scitation.org/doi/10.1116/1.4913294.

[14] Prakash, A. *et al.* Hybrid molecular beam epitaxy for the growth of stoichiometric BaSnO3. *Journal of Vacuum Science & Technology A* **33**, 060608 (2015). URL https://avs.scitation.org/doi/10.1116/1.4933401.

[15] Novoselov, K. S. *et al.* Electric Field Effect in Atomically Thin Carbon Films. *Science* **306**, 666–669 (2004). URL https://science.sciencemag.org/content/306/5696/666.

[16] Geim, A. K. & Novoselov, K. S. The rise of graphene. *Nature Materials* **6**, 183–191 (2007). URL https://www.nature.com/articles/nmat1849.

[17] Geim, A. K. & Grigorieva, I. V. Van der Waals heterostructures. *Nature* **499**, 419–425 (2013). URL https://www.nature.com/articles/nature12385.

[18] Shi, W. *et al.* Superconductivity Series in Transition Metal Dichalcogenides by Ionic Gating. *Scientific Reports* **5**, 12534 (2015). URL https://www.nature.com/articles/srep12534.

[19] Qi, Y. *et al.* Superconductivity in Weyl semimetal candidate $MoTe_2$. *Nature Communications* **7**, 11038 (2016). URL https://www.nature.com/articles/ncomms11038.

[20] Saito, Y. *et al.* Superconductivity protected by spin–valley locking in ion-gated MoS_2. *Nature Physics* **12**, 144–149 (2016). URL https://www.nature.com/articles/nphys3580.

[21] Lu, J. *et al.* Full superconducting dome of strong Ising protection in gated monolayer WS2. *Proceedings of the National Academy of Sciences* **115**, 3551–3556 (2018). URL https://www.pnas.org/content/115/14/3551.

[22] Fatemi, V. *et al.* Electrically tunable low-density superconductivity in a monolayer topological insulator. *Science* eaar4642 (2018). URL http://science.sciencemag.org/content/early/2018/10/24/science.aar4642.

[23] Sajadi, E. *et al.* Gate-induced superconductivity in a monolayer topological insulator. *Science* **362**, 922–925 (2018). URL http://science.sciencemag.org/content/362/6417/922.

[24] Lu, J. M. *et al.* Evidence for two-dimensional Ising superconductivity in gated MoS2. *Science* **350**, 1353–1357 (2015). URL http://www.sciencemag.org/cgi/doi/10.1126/science.aab2277.

[25] Xi, X. *et al.* Ising pairing in superconducting NbSe 2 atomic layers. *Nature Physics* **12**, 139–143 (2016). URL http://www.nature.com/articles/nphys3538.

[26] Xi, X., Berger, H., Forró, L., Shan, J. & Mak, K. F. Gate Tuning of Electronic Phase Transitions in Two-Dimensional ${\mathrm{NbSe}}_{2}$. *Physical Review Letters* **117**, 106801 (2016). URL https://link.aps.org/doi/10.1103/PhysRevLett.117.106801.

[27] Ugeda, M. M. *et al.* Characterization of collective ground states in single-layer ${\mathrm{NbSe}}_{2}$. *Nature Physics* **12**, 92–97 (2016). URL https://www.nature.com/articles/nphys3527.

[28] Qian, X., Liu, J., Fu, L. & Li, J. Quantum spin Hall effect in two-dimensional transition metal dichalcogenides. *Science* **346**, 1344–1347 (2014). URL http://science.sciencemag.org/content/346/6215/1344.

[29] Wu, S. *et al.* Observation of the quantum spin Hall effect up to 100 kelvin in a monolayer crystal. *Science* **359**, 76–79 (2018). URL http://science.sciencemag.org/content/359/6371/76.

[30] Tang, S. *et al.* Quantum spin Hall state in monolayer 1T'-WTe_2. *Nature Physics* **13**, 683–687 (2017). URL https://www.nature.com/articles/nphys4174.

[31] Fei, Z. *et al.* Edge conduction in monolayer WTe_2. *Nature Physics* **13**, 677–682 (2017). URL https://www.nature.com/articles/nphys4091.

[32] Xu, S.-Y. *et al.* Electrically switchable Berry curvature dipole in the monolayer topological insulator WTe 2. *Nature Physics* **14**, 900 (2018). URL https://www.nature.com/articles/s41567-018-0189-6.

[33] Yan, Z., Song, F. & Wang, Z. Majorana Corner Modes in a High-Temperature Platform. *Physical Review Letters* **121**, 096803 (2018). URL https://link.aps.org/doi/10.1103/PhysRevLett.121.096803.

[34] Wang, Q., Liu, C.-C., Lu, Y.-M. & Zhang, F. High-Temperature Majorana Corner States. *Physical Review Letters* **121**, 186801 (2018). URL https://link.aps.org/doi/10.1103/PhysRevLett.121.186801.

[35] Nayak, C., Simon, S. H., Stern, A., Freedman, M. & Das Sarma, S. Non-Abelian anyons and topological quantum computation. *Reviews of Modern Physics* **80**, 1083–1159 (2008). URL https://link.aps.org/doi/10.1103/RevModPhys.80.1083.

[36] Bosi, M. Growth and synthesis of mono and few-layers transition metal dichalcogenides by vapour techniques: a review. *RSC Advances* **5**, 75500–75518 (2015). URL https://pubs.rsc.org/en/content/articlelanding/2015/ra/c5ra09356b.

[37] Chhowalla, M. *et al.* The chemistry of two-dimensional layered transition metal dichalcogenide nanosheets. *Nature Chemistry* **5**, 263–275 (2013). URL https://www.nature.com/articles/nchem.1589.

[38] Vishwanath, S., Dang, P. & Xing, H. G. Challenges and Opportunities in Molecular Beam Epitaxy Growth of 2D Crystals. In *Molecular Beam Epitaxy*, 443–485 (Elsevier, 2018). URL https://linkinghub.elsevier.com/retrieve/pii/B9780128121368000177.

[39] Jia, Z.-Y. *et al.* Direct visualization of a two-dimensional topological insulator in the single-layer $1{T}^{\ensuremath{'}}\ensuremath{-}\mathrm{WT}{\mathrm{e}}_{2}$. *Physical Review B* **96**, 041108 (2017). URL https://link.aps.org/doi/10.1103/PhysRevB.96.041108, bibtex: ZYJiaPRB2017.

[40] Peng, L. *et al.* Observation of topological states residing at step edges of WTe 2. *Nature Communications* **8**, 659 (2017). URL https://www.nature.com/articles/s41467-017-00745-8.

[41] Kotekar-Patil, D., Deng, J., Wong, S. L., Lau, C. S. & Goh, K. E. J. Single layer MoS2 nanoribbon field effect transistor. *arXiv:1811.01390 [cond-mat]* (2018). URL http://arxiv.org/abs/1811.01390, arXiv: 1811.01390.

[42] El-Bana, M. S. *et al.* Superconductivity in two-dimensional NbSe 2 field effect transistors. *Superconductor Science and Technology* **26**, 125020 (2013). URL http://stacks.iop.org/0953-2048/26/i=12/a=125020.

[43] Cao, Y. *et al.* Quality Heterostructures from Two-Dimensional Crystals Unstable in Air by Their Assembly in Inert Atmosphere. *Nano Letters* **15**, 4914–4921 (2015). URL https://doi.org/10.1021/acs.nanolett.5b00648.

[44] Woods, J. M. *et al.* Suppression of Magnetoresistance in Thin WTe2 Flakes by Surface Oxidation. *ACS Applied Materials & Interfaces* **9**, 23175–23180 (2017). URL https://doi.org/10.1021/acsami.7b04934.

[45] Cucchi, I. *et al.* Microfocus Laser–Angle-Resolved Photoemission on Encapsulated Mono-, Bi-, and Few-Layer 1T'-WTe $_2$. *Nano Letters* **19**, 554–560 (2019). URL http://pubs.acs.org/doi/10.1021/acs.nanolett.8b04534.

[46] Ye, F. *et al.* Environmental Instability and Degradation of Single- and Few-Layer WTe2 Nanosheets in Ambient Conditions. *Small* **12**, 5802–5808 (2016). URL https://onlinelibrary.wiley.com/doi/abs/10.1002/smll.201601207.

[47] Jiao, L. *et al.* Molecular-beam epitaxy of monolayer MoSe 2 : growth characteristics and domain boundary formation. *New Journal of Physics* **17**, 053023 (2015). URL http://stacks.iop.org/1367-2630/17/i=5/a=053023.

[48] Hall, J. *et al.* Molecular beam epitaxy of quasi-freestanding transition metal disulphide monolayers on van der Waals substrates: a growth study. *2D Materials* **5**, 025005 (2018). URL http://stacks.iop.org/2053-1583/5/i=2/a=025005.

[49] Zhou, J. *et al.* Large-Area and High-Quality 2D Transition Metal Telluride. *Advanced Materials* **29**, n/a–n/a (2017). URL http://onlinelibrary.wiley.com/doi/10.1002/adma.201603471/abstract.

[50] Zhou, J. *et al.* A library of atomically thin metal chalcogenides. *Nature* **556**, 355–359 (2018). URL https://www.nature.com/articles/s41586-018-0008-3.

[51] Li, J., Cheng, S., Liu, Z., Zhang, W. & Chang, H. Centimeter-Scale, Large-Area, Few-Layer 1T'-WTe $_2$ Films by Chemical Vapor Deposition and Its Long-Term Stability in Ambient Condition. *The Journal of Physical Chemistry C* **122**, 7005–7012 (2018). URL http://pubs.acs.org/doi/10.1021/acs.jpcc.8b00679.

[52] Zhou, Y. *et al.* Direct Synthesis of Large-Scale WTe2 Thin Films with Low Thermal Conductivity. *Advanced Functional Materials* **27**, 1605928 (2017). URL https://onlinelibrary.wiley.com/doi/abs/10.1002/adfm.201605928.

[53] Tiefenbacher, S., Pettenkofer, C. & Jaegermann, W. Moiré pattern in LEED obtained by van der Waals epitaxy of lattice mismatched WS2/MoTe2(0001) heterointerfaces. *Surface Science* **450**, 181–190 (2000). URL http://www.sciencedirect.com/science/article/pii/S0039602800002971.

[54] Manzeli, S., Ovchinnikov, D., Pasquier, D., Yazyev, O. V. & Kis, A. 2D transition metal dichalcogenides. *Nature Reviews Materials* **2**, 17033 (2017). URL https://www.nature.com/articles/natrevmats201733.

[55] Zhou, Y. *et al.* Pressure-induced Td to 1T' structural phase transition in WTe2. *AIP Advances* **6**, 075008 (2016). URL https://aip.scitation.org/doi/full/10.1063/1.4959026.

[56] Cui, J. *et al.* Transport evidence of asymmetric spin–orbit coupling in few-layer superconducting 1 T d -MoTe 2. *Nature Communications* **10**, 2044 (2019). URL https://www.nature.com/articles/s41467-019-09995-0.

[57] Shi, Y. *et al.* Imaging quantum spin Hall edges in monolayer WTe2. *Science Advances* **5**, eaat8799 (2019). URL http://advances.sciencemag.org/content/5/2/eaat8799.

[58] Lüpke, F. *et al.* Coexistence of quantum spin hall edge state and proximity-induced superconducting gap in monolayer 1T'-WTe$_2$. *arXiv:1903.00493 [cond-mat]* (2019). URL http://arxiv.org/abs/1903.00493, arXiv: 1903.00493.

[59] He, Q. L. *et al.* Chiral Majorana fermion modes in a quantum anomalous Hall insulator–superconductor structure. *Science* **357**, 294–299 (2017). URL http://science.sciencemag.org/content/357/6348/294.

[60] Maeda, H., Tanaka, Y., Fukutomi, M. & Asano, T. A New High-Tc Oxide Superconductor without a Rare Earth Element. *Japanese Journal of Applied*

Physics **27**, L209 (1988). URL https://iopscience.iop.org/article/10.1143/JJAP.27.L209/meta.

[61] Wang, E. *et al.* Fully gapped topological surface states in Bi2Se3 films induced by a d-wave high-temperature superconductor. *Nature Physics* **9**, 621–625 (2013). URL http://www.nature.com/articles/nphys2744.

[62] Yilmaz, T. *et al.* Absence of a Proximity Effect for a Thin-Films of a Bi2Se3 Topological Insulator Grown on Top of a $Bi_2Sr_2CCu_2O_{8+}$ Cuprate Superconductor. *Physical Review Letters* **113**, 067003 (2014). URL https://link.aps.org/doi/10.1103/PhysRevLett.113.067003.

[63] Herman, M. A. & Sitter, H. *Molecular beam epitaxy: fundamentals and current status*. No. 7 in Springer series in materials science (Springer, Berlin ; New York, 1996), 2nd, rev. and updated ed edn.

[64] Engel-Herbert, R. Molecular beam epitaxy of complex oxides. In *Molecular Beam Epitaxy*, 417–449 (Elsevier, 2013). URL https://linkinghub.elsevier.com/retrieve/pii/B9780123878397000178.

[65] Koma, A. Van der Waals epitaxy for highly lattice-mismatched systems. *Journal of Crystal Growth* **201-202**, 236–241 (1999). URL http://www.sciencedirect.com/science/article/pii/S0022024898013293.

[66] Koma, A., Sunouchi, K. & Miyajima, T. Fabrication and characterization of heterostructures with subnanometer thickness. *Microelectronic Engineering* **2**, 129–136 (1984). URL http://www.sciencedirect.com/science/article/pii/0167931784900571.

[67] Koma, A. Van der Waals epitaxy—a new epitaxial growth method for a highly lattice-mismatched system. *Thin Solid Films* **216**, 72–76 (1992). URL http://www.sciencedirect.com/science/article/pii/0040609092908729.

[68] Koma, A., Ueno, K. & Saiki, K. Heteroepitaxial growth by Van der Waals interaction in one-, two- and three-dimensional materials. *Journal of Crystal Growth* **111**, 1029–1032 (1991). URL http://www.sciencedirect.com/science/article/pii/002202489191126U.

[69] Ueno, K., Saiki, K., Shimada, T. & Koma, A. Epitaxial growth of transition metal dichalcogenides on cleaved faces of mica. *Journal of Vacuum Science & Technology A* **8**, 68–72 (1990). URL https://avs.scitation.org/doi/10.1116/1.576983.

[70] Ueno, K., Shimada, T., Saiki, K. & Koma, A. Heteroepitaxial growth of layered transition metal dichalcogenides on sulfur-terminated GaAs{111} surfaces. *Applied Physics Letters* **56**, 327–329 (1990). URL https://aip.scitation.org/doi/10.1063/1.102817.

[71] Hertz, H. Ueber einen Einfluss des ultravioletten Lichtes auf die electrische Entladung. *Annalen der Physik* **267**, 983–1000 (1887). URL https://onlinelibrary.wiley.com/doi/abs/10.1002/andp.18872670827.

[72] Einstein, A. Über einen die Erzeugung und Verwandlung des Lichtes betreffenden heuristischen Gesichtspunkt. *Annalen der Physik* **322**, 132–148 (1905). URL http://doi.wiley.com/10.1002/andp.19053220607.

[73] Hüfner, S. *Photoelectron Spectroscopy: Principles and Applications*. Advanced Texts in Physics (Springer-Verlag, Berlin Heidelberg, 2003), 3 edn. URL https://www.springer.com/de/book/9783540418023.

[74] Carlson, T. A. & McGuire, G. Study of the x-ray photoelectron spectrum of tungsten—tungsten oxide as a function of thickness of the surface oxide layer. *Journal of Electron Spectroscopy and Related Phenomena* **1**, 161–168 (1972). URL https://linkinghub.elsevier.com/retrieve/pii/036820487280029X.

[75] Seah, M. P. & Dench, W. A. Quantitative electron spectroscopy of surfaces: A standard data base for electron inelastic mean free paths in solids. *Surface and Interface Analysis* **1**, 2–11 (1979). URL https://onlinelibrary.wiley.com/doi/abs/10.1002/sia.740010103.

[76] Powell, C. The Physical Basis for Quantitative Surface Analysis by Auger Electron Spectroscopy and X-Ray Photoelectron Spectroscopy. In *Quantitive Surface Analysis of Materials* (ed. McIntyre, N.), 5–5–26 (ASTM International, 100 Barr Harbor Drive, PO Box C700, West Conshohocken, PA 19428-2959, 1978). URL http://www.astm.org/doiLink.cgi?STP25597S.

[77] Oura, K. *Surface science: an introduction ; with 16 tables* (Springer, Berlin, 2003). OCLC: 249200082.

[78] Egerton, R. F. *Physical Principles of Electron Microscopy: An Introduction to TEM, SEM, and AEM* (Springer, New York, NY, UNITED STATES, 2011). URL http://ebookcentral.proquest.com/lib/eth/detail.action?docID=264884.

[79] Woodruff, D. P. Surface Microscopies (2016). URL /core/books/modern-techniques-of-surface-science/surface-microscopies/D559E0F7E279B1806FE87D56CD21B044.

[80] Pang, G. K. H., Baba-Kishi, K. Z. & Patel, A. Topographic and phase-contrast imaging in atomic force microscopy. *Ultramicroscopy* **81**, 35–40 (2000). URL http://www.sciencedirect.com/science/article/pii/S0304399199001643.

[81] García, R., Magerle, R. & Perez, R. Nanoscale compositional mapping with gentle forces. *Nature Materials* **6**, 405–411 (2007). URL https://www.nature.com/articles/nmat1925.

[82] AC160TS-R3 (????). URL https://afmprobes.asylumresearch.com/ac160ts-r3.html.

[83] Principal Features (????). URL https://www.haynesintl.com/alloys/alloy-portfolio_/High-temperature-Alloys/haynes-214-alloy.

[84] Lai, K. K. & Lamb, H. H. Tungsten chemical vapor deposition using tungsten hexacarbonyl: microstructure of as-deposited and annealed films. *Thin Solid Films* **370**, 114–121 (2000). URL http://www.sciencedirect.com/science/article/pii/S0040609000009433.

[85] Kwon, S., Vidic, R. & Borguet, E. Enhancement of adsorption on graphite (HOPG) by modification of surface chemical functionality and morphology. *Carbon* **40**, 2351–2358 (2002). URL http://www.sciencedirect.com/science/article/pii/S0008622302001550.

[86] Liu, H. J. *et al.* Molecular-beam epitaxy of monolayer and bilayer WSe 2 : a scanning tunneling microscopy/spectroscopy study and deduction of exciton binding energy. *2D Materials* **2**, 034004 (2015). URL http://stacks.iop.org/2053-1583/2/i=3/a=034004.

[87] Mullins, D. R. & Lyman, P. F. Sulfur-induced changes in the W(001) surface core level shift. *Surface Science* **285**, L473–L478 (1993). URL http://www.sciencedirect.com/science/article/pii/003960289390903W.

[88] NIST X-ray Photoelectron Spectroscopy (XPS) Database Main Search Menu (????). URL https://srdata.nist.gov/xps/main_search_menu.aspx.

[89] Biloen, P. & Pott, G. T. X-ray photoelectron spectroscopy study of supported tungsten oxide. *Journal of Catalysis* **30**, 169–174 (1973). URL http://www.sciencedirect.com/science/article/pii/0021951773900638.

[90] Walsh, L. A. *et al.* W Te 2 thin films grown by beam-interrupted molecular beam epitaxy. *2D Materials* **4**, 025044 (2017). URL http://stacks.iop.org/2053-1583/4/i=2/a=025044.

[91] WebCrossSections (????). URL https://vuo.elettra.eu/services/elements/WebElements.html.

[92] Lee, W.-Y. & Geiss, R. H. Degradation of thin tellurium films. *Journal of Applied Physics* **54**, 1351–1357 (1983). URL https://aip.scitation.org/doi/abs/10.1063/1.332156.

[93] Musket, R. G. Studies of clean and oxidized tellurium surfaces. *Surface Science* **74**, 423–435 (1978). URL http://www.sciencedirect.com/science/article/pii/0039602878900377.

[94] Zach, M. P., Ng, K. H. & Penner, R. M. Molybdenum Nanowires by Electrodeposition. *Science* **290**, 2120–2123 (2000). URL https://science.sciencemag.org/content/290/5499/2120.

[95] Favier, F., Walter, E. C., Zach, M. P., Benter, T. & Penner, R. M. Hydrogen Sensors and Switches from Electrodeposited Palladium Mesowire Arrays. *Science* **293**, 2227–2231 (2001). URL https://science.sciencemag.org/content/293/5538/2227.

[96] Walter, E. C. *et al.* Metal Nanowire Arrays by Electrodeposition. *ChemPhysChem* **4**, 131–138 (2003). URL https://onlinelibrary.wiley.com/doi/abs/10.1002/cphc.200390022.

[97] Niimi, Y. *et al.* Scanning tunneling microscopy and spectroscopy of the electronic local density of states of graphite surfaces near monoatomic step edges. *Physical Review B* **73**, 085421 (2006). URL https://link.aps.org/doi/10.1103/PhysRevB.73.085421.

[98] Tiefenbacher, S., Pettenkofer, C. & Jaegermann, W. Van Der Waals Epitaxy of Transition Metal Dichalcogenides Using Metal Organic Precursors (Movdwe). *MRS Online Proceedings Library Archive* **441** (1996). URL https://doi.org/10.1557/PROC-441-591.

[99] Gong, Y. *et al.* Tellurium-Assisted Low-Temperature Synthesis of MoS2 and WS2 Monolayers. *ACS Nano* **9**, 11658–11666 (2015). URL https://doi.org/10.1021/acsnano.5b05594.

[100] Powell, C. & Jablonski, A. *NIST Electron Inelastic-Mean-Free-Path Database*, vol. SRD 71 (National Institute of Standards and Technology, Gaithersburg MD, 2010), version 1.2 edn. URL https://www.nist.gov/srd/nist-standard-reference-database-71.

[101] J. -J. Yeh. *Atomic calculation of photoionization cross-sections and asymmetry parameters* (Gordon and Breach Science Publishers, Langhorne, Pennsylvania [etc., 1993).

[102] Reilman, R. F., Msezane, A. & Manson, S. T. Relative intensities in photoelectron spectroscopy of atoms and molecules. *Journal of Electron Spectroscopy and Related Phenomena* **8**, 389–394 (1976). URL http://www.sciencedirect.com/science/article/pii/0368204876800254.

[103] Tresback, J. Conversation with Jason Tresback (Center of Nanoscale Science) about AFM measurments (2019).

[104] Flitsch, F. A., Swanson, J. R. & Friend, C. M. Thermal and photoinduced decomposition of W(CO)6 on W(110). *Surface Science* **245**, 85–95 (1991). URL http://www.sciencedirect.com/science/article/pii/003960289190470D.

[105] Zaera, F. Tungsten hexacarbonyl thermal decomposition on nickel(100) surfaces. *The Journal of Physical Chemistry* **96**, 4609–4615 (1992). URL https://doi.org/10.1021/j100190a086.

[106] Xu, M. & Zaera, F. Mechanistic studies of the thermal decomposition of metal carbonyls on Ni(100) surfaces in connection with chemical vapor deposition processes. *Journal of Vacuum Science & Technology A* **14**, 415–424 (1996). URL https://avs.scitation.org/doi/abs/10.1116/1.580099.

[107] Warren, A., Nylund, A. & Olefjord, I. Oxidation of tungsten and tungsten carbide in dry and humid atmospheres. *International Journal of Refractory Metals and Hard Materials* **14**, 345–353 (1996). URL http://www.sciencedirect.com/science/article/pii/S0263436896000273.

[108] Lee, C.-H. *et al.* Tungsten Ditelluride: a layered semimetal. *Scientific Reports* **5**, 10013 (2015). URL https://www.nature.com/articles/srep10013.

[109] Song, Y.-H. *et al.* Observation of Coulomb gap in the quantum spin Hall candidate single-layer 1 T '-WTe 2. *Nature Communications* **9**, 4071 (2018). URL https://www.nature.com/articles/s41467-018-06635-x.

[110] Jiang, Y. C., Gao, J. & Wang, L. Raman fingerprint for semi-metal WTe_2 evolving from bulk to monolayer. *Scientific Reports* **6**, 19624 (2016). URL https://www.nature.com/articles/srep19624.

[111] Kim, Y. *et al.* Anomalous Raman scattering and lattice dynamics in mono- and few-layer WTe2. *Nanoscale* **8**, 2309–2316 (2016). URL https://pubs.rsc.org/en/content/articlelanding/2016/nr/c5nr06098b.

[112] Hoefer, K., Becker, C., Wirth, S. & Hao Tjeng, L. Protective capping of topological surface states of intrinsically insulating Bi2Te3. *AIP Advances* **5**, 097139 (2015). URL https://aip.scitation.org/doi/full/10.1063/1.4931038.

[113] Wang, Q. *et al.* Large-scale uniform bilayer graphene prepared by vacuum graphitization of 6H-SiC(0001) substrates. *Journal of Physics: Condensed Matter* **25**, 095002 (2013). URL https://doi.org/10.1088%2F0953-8984%2F25%2F9%2F095002.